S2S Prediction in GFDL SPEAR: MJO Diversity and Teleconnections

Baoqiang Xiang 1, 2, Lucas Harris 1, Thomas L. Delworth 1, Bin Wang 3, Guosen Chen 4, Jan-Huey Chen 1,2, Spencer K. Clark 1, 5, William F. Cooke 1, 2, Kun Gao 1, 2, J. Jacob Huff 1, 2, Liwei Jia 1,2, Nathaniel C. Johnson 1, Sarah B. Kapnick 1, Feiyu Lu 1, 6, Colleen McHugh 1, 7, Yongqiang Sun 1,6, Mingjing Tong 1, Xiaosong Yang 1, Fanrong Zeng 1, Ming Zhao 1, Linjiong Zhou 1, 6, Xiaqiong Zhou 2, 8

1. NOAA/Geophysical Fluid Dynamics Laboratory, Princeton, New Jersey
2. University Corporation for Atmospheric Research, Boulder, Colorado
3. International Pacific Research Center, University of Hawaii, Hawaii
4. Earth System Modeling Center, Key Laboratory of Meteorological Disaster of Ministry of Education, Collaborative Innovation Center on Forecast and Evaluation of Meteorological Disasters, Nanjing University of Information Science and Technology, Nanjing, China
5. Vulcan Inc., Seattle, Washington
6. Cooperative Institute for Modeling the Earth System, Program in Oceanic and Atmospheric Sciences, Princeton University, New Jersey
7. Science Applications International Corporation, Reston, Virginia
8. Environmental Modeling Center, NOAA/NWS/NCEP

Revised version on Aug. 26, 2021

Corresponding author:
Dr. Baoqiang Xiang
Email: Baoqiang.xiang@noaa.gov

Early Online Release: This preliminary version has been accepted for publication in *Bulletin of the American Meteorological Society*, may be fully cited, and has been assigned DOI 10.1175/BAMS-D-21-0124.1. The final typeset copyedited article will replace the EOR at the above DOI when it is published.

A S2S prediction system was developed using the GFDL SPEAR model showing its capability in predicting MJO diversity and teleconnections.

Accepted for publication in *Bulletin of the American Meteorological Society*. DOI 10.1175/BAMS-D-21-0124.1.

Abstract

A subseasonal-to-seasonal (S2S) prediction system was recently developed using the GFDL SPEAR global coupled model. Based on 20-year hindcast results (2000-2019), the boreal wintertime (November-April) Madden-Julian Oscillation (MJO) prediction skill is revealed to reach 30 days measured before the anomaly correlation coefficient of the real-time multivariate (RMM) index drops to 0.5. However, when the MJO is partitioned into four distinct propagation patterns, the prediction range extends to 38, 31, and 31 days for the fast-propagating, slow-propagating, and jumping MJO patterns, respectively, but falls to 23 days for the standing MJO. A further improvement of MJO prediction requires attention to the standing MJO given its large gap with its potential predictability (15 days). The slow-propagating MJO detours southward when traversing the maritime continent (MC), and confronts the MC prediction barrier in the model, while the fast-propagating MJO moves across the central MC without this prediction barrier. The MJO diversity is modulated by stratospheric quasi-biennial oscillation (QBO): the standing (slow-propagating) MJO coincides with significant westerly (easterly) phases of QBO, partially explaining the contrasting MJO prediction skill between these two QBO phases.

The SPEAR model shows its capability, beyond the propagation, in predicting their initiation for different types of MJO along with discrete precursory convection anomalies. The SPEAR model skillfully predicts the observed distinct teleconnections over the North Pacific and North America related to the standing, jumping, and fast-propagating MJO, but not the slow-propagating MJO. These findings highlight the complexities and challenges of incorporating MJO prediction into the operational prediction of meteorological variables.

Accepted for publication in *Bulletin of the American Meteorological Society*. DOI 10.1175/BAMS-D-21-0124.1.

1. Introduction

A pioneering work by Xie et al. (1963) revealed a local oscillatory signal with a prominent 40-50 day period in the western Pacific that has strong modulation on tropical cyclone activities (also see (also see Li et al. 2018). Madden and Julian (1971, 1972) discovered a global-scale 40-50 day oscillatory mode with pronounced eastward propagation across the whole tropics, known as the Madden-Julian Oscillation (MJO), a planetary-scale intraseasonal mode characterized by slow eastward propagation over the tropics. The development and evolution of MJO involve interactions of convection, planetary boundary layer, wave dynamics, moisture, and radiation, and it is also significantly modified by multi-scale interaction and air-sea coupling. Given the complexity of MJO, many theories have been proposed to explain the essential processes responsible for its existence, scale selection, and propagation (e.g., Jiang et al. 2020; Zhang et al. 2020).

Compared to synoptic weather variability, the MJO has longer persistence and an oscillatory nature, highlighting the importance of MJO prediction for subseasonal-to-seasonal (S2S) predictions of climate and extreme weather events. For example, the prediction of MJO has been demonstrated to be critical for the medium-range to the subseasonal prediction of tropical cyclones (Jiang et al. 2018; Lee et al. 2018; Lee et al. 2020; Vitart 2009; Xiang et al. 2014). A skillful MJO prediction also benefits the prediction of phenomena including the North Atlantic Oscillation (Lin et al. 2010), atmospheric rivers (DeFlorio et al. 2018; Mundhenk et al. 2018), and the US precipitation (Nardi et al. 2020).

Dynamical models have become the primary tool for MJO prediction. Extensive exploration of the predictability of the MJO in dynamical models has achieved substantial advances in recent decades, while a big gap still remains between the prediction skill and the potential predictability (Kim et al. 2018; Kim et al. 2019; Neena et al. 2014; Vitart 2017). A myriad of factors influence

Accepted for publication in *Bulletin of the American Meteorological Society*. DOI 10.1175/BAMS-D-21-0124.1.

MJO prediction, each different among models, such as the convection parameterization (Zhu et al. 2020), air-sea coupling (Fu et al. 2013; Harris et al. 2020; Zhu and Kumar 2019), and initialization (Ren et al. 2016; Wu et al. 2020). Additionally, the stratospheric quasi-biennial oscillation (QBO) can rectify the MJO activities (MJO days) and propagation, and influence its prediction skill (Lim et al. 2019; Marshall et al. 2017; Martin et al. 2021; Wang et al. 2019b; Zhang and Zhang 2018). Some systematic biases in model mean states and feedback processes are shown to exert direct effects on the MJO prediction skill (Kim et al. 2019; Lim et al. 2018).

It is worth noting that individual MJO events vary markedly from event to event in their amplitude, life cycle, and propagation (Wang and Rui 1990). Kim et al. (2014) revealed that some MJO events propagate across the maritime continent (MC) while some others do not. About 40% of the observed MJO events are blocked by the MC (Kerns and Chen 2020). On the basis of the substantially different propagation features of individual MJO events, Wang et al. (2019a) separated the MJO events into four clusters using a clustering method (standing, jumping, slow-propagating, and fast-propagating events). The standing MJO is referring to the events with a locally oscillatory feature in the Indian Ocean without evident propagation. The jumping MJO represents the cases with a sudden migration of anomalous convection from the eastern Indian Ocean to the western Pacific. They claimed that their existence is controlled by different large-scale background mean states and interaction between tropical wave dynamics and convection. It prompts the question of whether the MJO prediction depends on the MJO propagation characteristic? The objective of this study is twofold: firstly, to introduce a recently developed prediction modeling system targeting S2S prediction; and secondly, to identify the potential skill dependence on MJO diversity using this prediction system.

Accepted for publication in *Bulletin of the American Meteorological Society*. DOI 10.1175/BAMS-D-21-0124.1.

The paper is organized as follows. Section 2 introduces the model, experiments, and methodology. Sections 3 and 4 describe the overall MJO prediction skill and the skill dependence on MJO diversity, respectively. Sections 5, 6, and 7 present the model prediction of MJO propagation, initial development, and teleconnections, respectively, in the context of MJO diversity. We end with a summary and discussion in section 8.

2. Model, hindcast experiments, and methodology

a. Model and hindcast experiments

We use the Geophysical Fluid Dynamics Laboratory (GFDL) Seamless System for Prediction and EArth system Research (SPEAR) coupled model. The model was developed as the next generation GFDL modeling system for seasonal to multidecadal prediction and projection (Bushuk et al. 2021; Delworth et al. 2020; Lu et al. 2020; Murakami et al. 2020). To approach the seamless suite of prediction, here, we extend the research focus to the S2S timescale. The SPEAR model shares many components with the GFDL CM4.0 model (Held et al. 2019). In particular, SPEAR uses an atmospheric and land model identical to AM4.0/LM4.0 (Zhao et al. 2018a; Zhao et al. 2018b) but with a dynamical vegetation model and a lower resolution MOM6 (Adcroft et al. 2019). There are three configurations of SPEAR that share the same ocean model (horizontal resolution of about 1^{o} and 75 vertical levels) but with three different atmospheric horizontal resolutions, which are referred to as SPEAR_LO (1°), SPEAR_MED (0.5°), and SPEAR_HI (0.25°). SPEAR_MED uses an 0.5 degree AM4.0, which contains 33 vertical levels with the top of the atmosphere at 1 hPa. The 0.5 degree AM4.0 has been documented in Zhao (2020). SPEAR_MED has been demonstrated to produce realistic simulations of extreme weather statistics such as the frequency of tropical cyclones (Murakami et al. 2020), atmospheric rivers (Zhao 2020), and

Accepted for publication in *Bulletin of the American Meteorological Society*. DOI 10.1175/BAMS-D-21-0124.1.

mesoscale convective systems (Dong et al. 2021). SPEAR_MED is used in this study for S2S prediction, and we refer to it as SPEAR hereinafter for simplicity. This model has shown a realistic MJO simulation from its control run (Delworth et al. 2020), offering an excellent opportunity to study the MJO prediction and some related issues. The reader is referred to Delworth et al. (2020) for additional details about this model.

Similar to Xiang et al. (2015), initial conditions for the atmosphere and ocean were generated through a simple nudging technique towards observations with several years' integration before prediction. The atmospheric nudging fields include winds, temperature, and specific humidity using the Modern-Era Retrospective Analysis for Research and Applications, version 2 (MERRA-2) analysis data (6-hourly interval) (Gelaro et al. 2017). The sea surface temperature (SST) is nudged to NOAA Optimum Interpolation 1/4 Degree Daily SST Analysis (OISST, v2) (Reynolds et al. 2007). Using the same SPEAR model, the ocean initialization for S2S prediction is much simpler than the seasonal-to-decadal prediction system that adopts a comprehensive ocean data assimilation system (Lu et al. 2020), allowing a later assessment of the potential roles of subsurface ocean initialization on S2S prediction. Hindcasts were carried out every five days from January 2000 to April 2019, and ten ensemble members were generated by using perturbed nudging strengths for both the atmosphere and the ocean SST so that they differ from one another in the initial conditions. The nudging of circulation is applied to the whole atmosphere. However, the nudging of moisture field is confined in the free atmosphere with the lowest several model layers (roughly the boundary layer) unperturbed, considering the fact that the moisture field in analysis data is relatively less reliable than other variables and the nudging of moisture within boundary layer may induce large initial shock in a coupled system via strongly altering latent heat flux. Since the MJO is most pronounced in boreal wintertime, we focus on the period from November to the

Accepted for publication in *Bulletin of the American Meteorological Society*. DOI 10.1175/BAMS-D-21-0124.1.

ensuing April. We made 708 hindcast events, and each has ten members. We integrated each hindcast for 45 days.

b. Methodology

The observational anomalies were obtained by removing the time mean and the first three harmonics of the observational climatological annual cycle and subtracting the time-mean anomalies over the previous 120 days. The hindcast anomalies are calculated by removing the model hindcast climatology and also the previous-120 days' time-mean anomalies.

The evaluation procedure for MJO prediction is similar to Xiang et al. (2015) and adopts the widely used Real-time Multivariate MJO (RMM) index (Wheeler and Hendon 2004) as a metric to measure the MJO and its prediction. The anomalies of outgoing longwave radiation (OLR) and 850 hPa and 200 hPa zonal winds are then projected onto two observed leading multivariate empirical orthogonal function (EOF) modes to obtain the RMM indices (Wheeler and Hendon 2004) (Figure S1). The first (second) mode represents the phases with anomalous convection in the Indian Ocean (western Pacific). The observed and predicted two RMM indices (RMM1 and RMM2) are then normalized by the standard deviation of the observed RMM indices. Using the above RMM indices as the predictands, the so-called bivariate anomaly correlation coefficient (ACC) and root mean square error (RMSE) were used here to measure its forecast skill following (Lin et al. 2008). The MJO amplitude is defined as $\sqrt{RMM1^2 + RMM2^2}$.

For verification, the data we used comprise the NOAA daily mean interpolated OLR data (Liebmann and Smith 1996) and ERA-5 reanalysis data as observations (C3S, 2017), including winds, two-meter air temperature (t2m), geopotential height, and specific humidity. All data are interpolated to 1°x1° resolution for analysis.

Accepted for publication in *Bulletin of the American Meteorological Society*. DOI 10.1175/BAMS-D-21-0124.1.

3. Overall evaluation of the MJO prediction

Figure 1a shows the bivariate ACC of MJO prediction in boreal wintertime (November to April) evaluated based on all the hindcasts (708 cases with 10 ensemble members). The mean skill from a single member is about 23 days, as determined by the maximum lead time with the ACC exceeding 0.5. As expected, the ACC for the 10-member ensemble-mean is superior to individual members, with a prediction skill of 30 days. The prediction skill is nearly saturated when using five ensemble members (29 days), and additional ensemble members add little to the MJO prediction skill (Figure S2). The ensemble spread is much smaller than the RMSE (Fig. 1b), indicating an under-dispersive ensemble that may limit the overall prediction skill of this system. The ten-member ensemble mean serves as the basis for all the following analyses, except where otherwise noted.

We further investigate the skill dependence on the MJO initial and target amplitude and phases. The skill has a much smaller difference between the initially strong (|RMM|>1) and weak (|RMM|<1) cases than the target strong and weak cases (Fig. 2a vs. 2c). Here, the target cases are referring to the MJO events during the forecast period. In other words, the skill is more sensitive to the target MJO amplitude during the forecast period than its initial amplitude. Note that some models experience strong sensitivity with initial amplitude, but some do not (Lim et al. 2018). The skill also differs among different MJO phases. A relatively higher skill is found when initiated at phases 3 and 4 with the anomalous wet phase in the eastern Indian Ocean and MC. In comparison, the skill is relatively lower during phases 1 and 2 when the anomalous intense convection occurs in the western and central Indian Ocean (Fig. 2b). The skill is higher for the target phases 3 and 4 than the target phases 5 and 6 (Fig. 2d). The above skill dependence on MJO amplitude and phase is generally similar to a previous version of the GFDL model (Xiang et al. 2015).

Accepted for publication in *Bulletin of the American Meteorological Society*. DOI 10.1175/BAMS-D-21-0124.1.

The MJO prediction skill is determined by the error growth in amplitude and propagation speed. Here we examine the MJO amplitude and its phase angle error for initially strong MJO cases (Fig. 3). The phase angle error is estimated between the observed and predicted RMM index following (Rashid et al. 2011). The predicted MJO amplitude agrees well with observation during the first ten days but then decreases very rapidly (Fig. 3a) along with the increase of noise. During the first 25 days, the predicted mean amplitude is comparable but slightly weaker (by 7.7%) than observations. The mean phase angle error in the first 25 days is -4.0° (Fig. 3c), with a magnitude generally smaller than 10.0° for individual phases (Fig. 3d). The individual member has a similar amplitude as observations (Fig. 3a), implying that the amplitude error from ensemble-mean is largely attributed to the rapid increase of noise. Compared with a previous version of the GFDL model (Xiang et al. 2015), the predicted amplitude error (phase angle error) in the first 25 days is reduced by 38% (5%), in agreement with an overall improved MJO prediction skill (30 days vs 27 days).

4. Skill dependence on MJO diversity

Given the contrasting propagation behaviors for individual MJO events, it is natural to question whether the MJO prediction is dependent on its propagation patterns. The first step to address this question is to identify individual MJO events. Following Wang et al. (2019a), an MJO event is selected when the area-averaged OLR anomalies in the equatorial Indian Ocean (75°E-95°E, 10°S-10°N) are negative and have an amplitude greater than one standard deviation for five successive days (roughly during the MJO phases 2 and 3). K-means cluster analysis (Kaufman and Rousseeuw 2009) is then applied to classify the MJO events based on their propagation patterns. This analysis identifies four types of MJO events: standing, jumping, slow-propagating, and fast-propagating

Accepted for publication in *Bulletin of the American Meteorological Society*. DOI 10.1175/BAMS-D-21-0124.1.

types (Wang et al. 2019a). Eventually, 55 MJO events were identified during the studied period from January 2000 to April 2019, including 12 standing, 14 jumping, 15 slow-propagating, and 14 fast-propagating cases (Table 1). Their contrasting propagation features are apparent from the composite OLR anomalies centered in the midpoint of the selected events (day 0) (Figs. 4c-f).

For each MJO cluster, we consider all the hindcasts initiated during the period between 20 days before and 15 days after the midpoint of the selected event (day 0), approximately covering the life cycle of the selected cases. Since the hindcasts are carried out every five days, the total forecast case numbers for these four groups are 88, 104, 116, and 92, respectively. Results show that the fast-propagating MJO possesses the best prediction skill of 38 days (Fig. 4a). The jumping MJO attains a similar prediction skill with the slow-propagating MJO (31 days), albeit the jumping MJO is categorized into the non-propagating group (Wang et al. 2019a). The standing MJO has the lowest skill (23 days). We conclude that the model tends to be more skillful in predicting the propagating and jumping MJO than the standing MJO.

The distinct MJO prediction skill among four clusters of MJO is possibly related to their potential predictability. Based on the perfect model assumption, the potential predictability can be estimated by taking one ensemble member as the truth and the ensemble-mean of the other members as predictions. The four clusters of MJO exhibit similar potential predictability (38-39 days) (Fig. 4b), which obviously cannot explain the contrasting prediction skill as shown in Fig. 4a. We also infer that there is much larger room to improve the prediction of the standing MJO than the other types of MJO, and a further MJO skill enhancement in SPEAR primarily relies on advancing the standing MJO prediction.

More insights into the skill dependence on MJO types can be gained by examining the relationship between the MJO prediction and its amplitude (Fig. 5a). For the standing (fast-

Accepted for publication in *Bulletin of the American Meteorological Society*. DOI 10.1175/BAMS-D-21-0124.1.

propagating) MJO, the initially weak cases have relatively lower (higher) skills than the initially strong cases. However, for both the jumping and slow-propagating MJO the model shows a comparable skill between the initially weak and strong cases. The skill spread among different groups of MJO tends to be larger for the initially weak cases than the initially strong cases. Intriguingly, a very similar skill is found for these four types of MJO when initiated at very strong MJO (|RMM| >1.5) (not shown). The MJO prediction is less sensitive to the target amplitude. The skill for target strong (weak) cases is around 35 (10) days for all four clusters of MJO (Figure S3). Therefore, the overall skill diversity (Fig. 4a) is primarily related to the skill difference for initially weak cases.

The observed MJO amplitude differs substantially among different types of MJO. Figure 5b displays the observational MJO amplitude for individual groups during the whole forecast period (45 days) by counting all the selected cases. The fast-propagating MJO has the strongest amplitude, followed by the slow-propagating, the jumping MJO, and the standing MJO, which has the smallest mean MJO amplitude. Given this, there are more weak cases for the standing MJO than the other groups, which may account for the overall lower skill for the standing MJO considering the skill-dependence on the amplitude. Compared to the fast-propagating MJO, the relatively lower skill for the slow-propagating MJO may reflect the MC prediction barrier effects (Kim et al. 2018; Weaver et al. 2011), and we will discuss this later.

One may wonder whether the relatively lower prediction skill for the standing MJO is related to the intrinsic limitation of the metrics used (bivariate ACC of RMM indices) that may not be appropriate to represent its standing feature in the Indian Ocean (Fig. 4c). To address this, we examine the prediction skill of convection and circulation anomalies in the equatorial Indian Ocean

Accepted for publication in *Bulletin of the American Meteorological Society*. DOI 10.1175/BAMS-D-21-0124.1.

(Figure S4). The skill difference among the four MJO types is broadly consistent with that based on the bivariate ACC (Figure s4 versus Fig. 4a), confirming the robustness of the results.

5. Prediction of MJO propagation diversity and its interannual modulations

5.1 Prediction of the diverse MJO propagations and the underlying mechanisms

Figure 6 compares the observed and predicted equatorial (10°S-10°N) propagation features of MJO initiated five days before the peak phase in the equatorial Indian Ocean (day -5). The broad features of the observed standing, jumping, slow- and fast-propagating MJO events (top two rows) are predicted reasonably well when initiated at day -5 (bottom two rows) despite an underpredicted amplitude. One noticeable deficiency is the underpredicted propagation speed for the slow-propagating MJO initiated at day -5. The predicted convective anomalies gradually fade when reaching the MC without further propagation to the western Pacific (Fig. 6). For the slow-propagating MJO, the issue of underpredicted convection anomalies tends to be more severe when initiated at day -10, together with a too slow propagation (Figure S5). This is partially responsible for the lower prediction skill than the fast-propagating MJO.

Extensive studies have been conducted to study the mechanisms for MJO propagations. One group accentuates the role of preconditioning characterized by lower-tropospheric moistening ahead of major convection (Benedict and Randall 2007; Hsu and Li 2012; Kiladis et al. 2005; Wang and Lee 2017). Figure 6 shows that for the standing and jumping MJO, the lower-tropospheric convergence and moistening are in phase with the convective anomalies in the Indian Ocean, cohesive with their rather stationary feature in the Indian Ocean. For the jumping MJO, the anomalous convergence and moistening in the MC even slightly lead the major convection in the Indian Ocean, providing a pathway for the fast transition of convection from the Indian Ocean to

Accepted for publication in *Bulletin of the American Meteorological Society*. DOI 10.1175/BAMS-D-21-0124.1.

the western Pacific. For both the slow and fast-propagating MJO, there is an evident premoistening characterized by lower-tropospheric convergence and moistening located to the east of the major deep convection. The model prediction qualitatively agrees with observations, while the low-tropospheric convergence almost disappears to the east of 150°E for all groups of MJO suggestive of a systematic model bias.

The premoistening is predominantly driven by the lower-tropospheric moisture convergence that is related to the Kelvin wave and the resultant equatorial low-pressure at the top of the boundary layer (Haertel 2021; Hsu and Li 2012; Wang 1988; Wang and Lee 2017). Note that the convergence anomalies are mainly ascribable to zonal winds rather than meridional winds. We present, in Figure 7, the spatial patterns of OLR, 850 hPa winds, and 850 hPa geopotential height anomalies. The model prediction initiated at day -5 generally resembles the observed characteristics for these four groups of MJO (Fig. 7).

Some indigenous features are identified among these four groups from observations (Fig. 7). The easterly wind anomalies over the MC and western Pacific are much weaker for the standing MJO than the other three groups. Given the strong zonal gradient of climatological moisture in the Indian Ocean, the westerly wind anomalies as a Rossby wave response induce a negative moisture advection and deteriorate the convection anomalies (Adames and Kim 2016), facilitating its phase transition. Meanwhile, the increased atmospheric stability due to convective heating and the resultant decreased SST also contribute to its phase transition. The above physical processes represent a discharge-recharge process responsible for its local oscillatory feature (Bladé and Hartmann 1993). The jumping MJO possesses a weak Rossby wave response but with a far-reaching Kelvin wave component. Unlike the propagating MJO, the jumping MJO's easterly anomalies are confined in the western Pacific without penetrating the MC. The newly formed

Accepted for publication in *Bulletin of the American Meteorological Society*. DOI 10.1175/BAMS-D-21-0124.1.

convection anomalies in the western Pacific are relatively independent of the preceding major convection in the Indian Ocean (Fig. 7). Another notable difference is that the drying anomalies in the MC and western Pacific are significantly weaker for both the standing and jumping MJO than the propagating MJO, which may have some consequences on the MJO propagation (Kim et al. 2014). For the fast-propagating MJO, the major convection is coupled to the strong Kelvin waves during the whole period when traversing the MC (Fig. 7). It has a rather meridionally symmetric pattern of anomalous convection during the first week. The major convection even migrates to the Northern Hemisphere together with a northwest-southeast tilted structure at weeks 2 and 3.

The observed and predicted features for different kinds of MJO suggest that the tropical wave dynamics and its interaction with the lower-tropospheric moisture may play an important role in MJO propagation, a point emphasized by the so-called convection-dynamics-moisture trio-interaction theory (Wang et al. 2016). However, it is also noticed that for the slow-propagating MJO, the anomalous moisture anomalies tend to decouple from the Kelvin wave during week 3, accompanied by southeastward detouring convection-circulation anomalies to the south of MC. We argue that some other processes may contribute to its further eastward propagation from observations for the slow-propagating MJO, such as the horizontal advection (Kim et al. 2017) or wind-induced surface heat exchange (WISHE) given the mean westerly winds in this region. However, the model presumably has difficulty capturing these possible processes, leading to the rapid termination of MJO in the eastern MC (Figs. 6, 7). It is concluded that the slow-propagating MJO suffers the MC prediction barrier from model predictions, while the fast-propagating MJO seemingly does not have this problem. The fast-propagating MJO has a larger zonal scale than the slow-propagating event, contributing to its faster propagation speed (Adames and Kim 2016; Chen and Wang 2020).

Accepted for publication in *Bulletin of the American Meteorological Society.* DOI 10.1175/BAMS-D-21-0124.1.

5.2 Observed and predicted impacts of ENSO and QBO on MJO diversity

What are the root causes for the diversified propagation for different types of MJO? Why are the equatorial waves so different for different types of MJO? One possibility is due to the regulation of interannual variability (Fig. 8). Here interannual variability is approximately estimated as the difference between the averaged 30-day unfiltered anomalies and the averaged 30-day anomalies with the previous 120-day anomalies removed. Wang et al. (2019a) found that the standing (fast-propagating) MJO is related to a La Nina (central Pacific El Nino) background mean state, while no statistically significant SST anomalies are found in the equatorial Pacific. The results are overall consistent with Wang et al. (2019a) but we also notice there is a significant SST cooling in the far eastern Pacific for the slow-propagating MJO (Fig. 8c), a signature of an increased zonal SST gradient similar to that for the fast-propagating MJO (Fig. 8d). The convection anomalies are dynamically coherent with the lower-boundary SST changes for different clusters of MJO. The modulation of El Nino/Southern Oscillation (ENSO) on MJO is arguably through two processes: the resultant expansion/shrinkage of the warm pool area that may alter the spatial scale of MJO (Lyu et al. 2021; Wang et al. 2019a), and the change of mean moisture and vertical shear over the MC (Jia et al. 2020; Wei and Ren 2019).

Besides ENSO, the role of stratospheric QBO on the MJO activities (MJO frequency, duration, amplitude, and propagation) has been articulated recently given the tight QBO-MJO connection in boreal wintertime (Liu et al. 2014; Yoo and Son 2016; Zhang and Zhang 2018). The QBO-MJO coupling becomes even more prominent in recent decades (Klotzbach et al. 2019). Here we found that the occurrence of standing MJO coincides with significant westerly QBO phases (WQBO) (Fig. 8e), in agreement with the conclusion that there is more MC barrier effect during WQBO

Accepted for publication in *Bulletin of the American Meteorological Society*. DOI 10.1175/BAMS-D-21-0124.1.

than EQBO (Zhang and Zhang 2018). The occurrence of slow-propagating MJO is related to significant easterly QBO phases (EQBO) (Fig. 8g). However, there is no significant relationship between the QBO and the other two clusters of MJO (this conclusion is valid even for the December-February when the QBO-MJO connection is most robust) (Fig. 8f and 8h).

The model accurately predicts the corresponding interannual variability associated with ENSO and QBO (Figure S6). Similar to the literature (Lim et al. 2019; Marshall et al. 2017), the impacts of QBO on the MJO prediction skill is clearly shown with a higher prediction skill during EQBO than WQBO (31 vs 27 days) (Figure S7). This is also consistent with the finding that the model has better prediction skills for the slow-propagating MJO than the standing MJO (Fig. 4a). Regarding the physical mechanisms to explain the role of QBO on MJO, several possible mechanisms have been proposed including the upper-tropospheric stability, cloud radiative feedbacks, QBO wind anomalies, and the changes to wave propagation (Martin et al. 2021; Yoo and Son 2016; Zhang and Zhang 2018). However, they remain largely untested and there is no consensus on a particular mechanism that can explain all the observed QBO-MJO connections. About how QBO modulates these four types of MJO is an open question. Given the limited sample size of MJO cases (Table 1), the robustness needs to be confirmed by considering more MJO cases.

6. Predicting the initial development and identifying the precursors

This section focuses on understanding the predictability of the initial development in the Indian Ocean and identifying its potential precursors. First, we assessed the model's skill in predicting the target peak phase of MJO (around day 0) with different lead times (Fig. 9). For the standing MJO, the anomalous enhanced convection in the Indian Ocean is highly predictable even with a

Accepted for publication in *Bulletin of the American Meteorological Society*. DOI 10.1175/BAMS-D-21-0124.1.

20-day lead time. For the jumping MJO, the predicted active convection in the eastern Indian Ocean is weak and less robust for a 20-day lead forecast. The prediction of the second convection center in the western Pacific is even more challenging, and both the 15- and 20-day lead forecasts fail to capture it. For both the slow and fast-propagating MJO, the drying anomalies in the western Pacific are less predictable than the wetting anomalies in the Indian Ocean. One issue for the slow-propagating MJO is that the westerly wind anomalies to the west of the convection center are substantially underpredicted. This may contribute to the slowdown of its eastward propagation because of the associated underestimated zonal moisture advection. Note that the selected cases are not completely the same at different lead times given the data availability from model hindcasts.

Why does the model have the ability in predicting the initial development of diversified MJO? What are the precursory signals for these four types of MJO? We further examine the time evolution of preceding convection and circulation anomalies from observations (Fig. 10). As a common precursor for all types of MJO, the prevailing easterly wind anomalies in the Indian Ocean drive the coupled system more subtly towards a state in which the anomalous convection is favored in the Indian Ocean (Fig. 10). The convection anomalies exhibit distinctive precursory conditions that may distinguish the occurrence of different types of MJO. For the standing MJO, pronounced drying anomalies cover nearly the whole tropical Indian Ocean between day -20 and day -10 (Fig. 10, green boxes in the first column), which decay rapidly from day -15 to day -10 before the onset of the wet phase at around day -10. This indicates that the wet phase is preceded by a local dry phase as an oscillatory mode. For the jumping MJO, relatively small-scale convection anomalies are detected in the southern central equatorial Indian Ocean (Fig. 10, green boxes in the second column), and the resultant easterly winds anomalies are responsible for the onset of the wet phase of MJO in the southwest Indian Ocean.

Accepted for publication in *Bulletin of the American Meteorological Society*. DOI 10.1175/BAMS-D-21-0124.1.

The slow-propagating MJO displays a significant dry phase in the central-to-eastern Indian Ocean during the period between day -20 and day -10 (Fig. 10, green boxes in the third column), which exhibits a clear eastward propagation across the MC to the western Pacific. Note that the dry phase does not show the southward detouring feature near the MC distinguished from its wet phase. For the fast-propagating MJO, the major loading of suppressed convection is anchored in the MC and western Pacific (Fig. 10, green boxes in the fourth column) without an apparent propagation before the initial development of the wet phase in the Indian Ocean. Given the distinctive time evolution of the convection anomalies (Fig. 10), it is inferred that the standing and slow-propagating MJO are mostly "successive MJO", while the jumping and fast-propagating MJO are mainly "primary MJO". Here the "successive MJO" is referring to the cases with a preceding event and the "primary MJO" represents the cases originating from the Indian Ocean (Matthews 2008). The model generally predicts a similar time evolution of convection and circulation anomalies as observations for all types of MJO when initiated at day -20 (Fig. 10).

7. Prediction of teleconnections

The impacts of the MJO are not just within the tropics but also in the extratropics as well. The MJO's extratropical circulation signature has been studied extensively, and many efforts have been made to unravel the physical processes that underlie the establishment of the teleconnections forced by MJO (Ferranti et al. 1990; Stan et al. 2017; Tseng et al. 2019). However, many current climate models still have difficulty in realistically simulating MJO, and the error in the Pacific subtropical jet greatly limits the ability to faithfully produce the MJO teleconnection patterns (Henderson et al. 2017; Wang et al. 2020). A skillful prediction of the relevant tropical convection could allow the prediction of its remote teleconnections to become possible.

Accepted for publication in *Bulletin of the American Meteorological Society*. DOI 10.1175/BAMS-D-21-0124.1.

Chen (2021) has examined the observational circulation anomalies associate with these four types of MJO. Here one example is shown to illustrate the observed and predicted distinctive t2m and 500 hPa geopotential height anomalies (averaged 11-20-day after day 0) associated with these four types of MJO by focusing on the Pacific-North America sector (Fig. 11). For the standing MJO, robust cold t2m anomalies are observed near the Chukchi Sea, northern Canada, and the adjacent seas (Fig. 11a). The jumping MJO excites a zonal wave-train circulation over the northeastern Pacific-North America-North Atlantic sector, with a coherent zonal dipole pattern of t2m anomalies in North America and a significant warming over the Greenland Sea and Norwegian Sea regions (Fig. 11b). The slow- and fast-propagating MJO have a similar teleconnection pathway in the Pacific-North America sector, reminiscent of a typical pattern of the North Pacific Oscillation (NPO) mode with a low-pressure system over Alaska and the Bering Sea and high pressure in northern North America (Rogers 1981). Compared to the slow-propagating MJO, the fast-propagating MJO induces a slightly southward shifted warming in North America (Fig. 11d vs. 11c). For the fast-propagating MJO, the circulation and surface temperature anomalies in the North Atlantic sector project onto the positive phase of North Atlantic Oscillation (NAO) (Fig. 11d), as documented in many previous studies (Cassou 2008; Lin et al. 2009). It is of interest to note that the teleconnections associated with the standing and propagating MJO resemble very similar patterns with two leading EOF modes of the wintertime cold extremes in North America (Xiang et al. 2020). This implies that the MJO is one of the major drivers and also a key predictability source for the wintertime extremes in North America but that the occurrence of such extremes may be sensitive to the MJO type.

The remarkable teleconnection differences highlight the importance of accurately predicting the propagation characteristic of MJO in the tropics. Inspection of the model hindcasts initiated at

Accepted for publication in *Bulletin of the American Meteorological Society*. DOI 10.1175/BAMS-D-21-0124.1.

around day 0 (strongest convection in the Indian Ocean) reveals a considerable skill in predicting the distinguished circulation and temperature anomalies for the standing, jumping, and fast-propagating MJO (Fig. 11). However, the model struggles to predict the teleconnections associated with the slow-propagating MJO (Fig. 11g). The corresponding pattern correlations between the observed and predicted t2m anomalies are 0.57 (standing), 0.64 (jumping), 0.19 (slow-propagating), and 0.55 (fast-propagating), respectively. We also examined the same time period as in Fig. 11 but initiated at day -5 and found that the model has some skill in predicting the associated teleconnections for the standing and fast-propagating MJO, while the model is limited in its ability to predict the teleconnections for both the jumping and slow-propagating MJO (not shown). The detailed processes leading to the limited skill in predicting its teleconnection remain elusive and require further investigation.

8. Summary and discussion

8.1 Conclusion

Improvements in MJO prediction skills are critical for developing prediction products for various weather phenomena. This study introduces a newly developed S2S prediction system using the GFDL SPEAR global coupled model. The wintertime (November-April) MJO prediction is evaluated using 20-year hindcasts (2000-2019). Results show that the model skillfully predicts the MJO for 30 days before the bivariate ACC of the RMM index drops to 0.5 (Fig. 1). The MJO prediction skill is dependent on the MJO propagation features (Fig. 4). The fast-propagating MJO has the best skill of 38 days, followed by the slow-propagating MJO and jumping MJO (31 days), and then the standing MJO (23 days). The diversified skills for different types of MJO are related to their contrasting skills initiated at weak MJO and their amplitude difference (Fig. 5). To further

Accepted for publication in *Bulletin of the American Meteorological Society*. DOI 10.1175/BAMS-D-21-0124.1.

improve the MJO prediction in SPEAR, the key is to advance the prediction of standing MJO given its large gap with its potential predictability (15 days) (Fig 4). The slow-propagating MJO detours southward when traversing the MC and suffers the MC prediction barrier effect, while the fast-propagating MJO propagates across the central MC without the MC prediction barrier issue (Figs. 6, 7). The intensity of Kelvin waves and the zonal spatial scales, potentially modulated by the background interannual variability, are essential in determining their different propagations (Figs. 7, 8). The MJO diversity is modulated by interannual variabilities from ENSO and QBO. In particular, we found that the occurrence of the standing MJO coincides with significant WQBO phases and the slow-propagating MJO is corresponding to significant EQBO phases. The modulation of QBO on MJO diversity partially explains the contrasting MJO prediction skill between two QBO phases.

The SPEAR model exhibits its capability not only in predicting the diversified MJO propagation (Figs. 6, 7) but also in predicting its initial development in the Indian Ocean (Fig. 9) accompanying by contrasting precursory convection signals (Fig. 10). Distinct teleconnections in the northern extratropics are revealed for these four types of MJO, and the SPEAR model realistically predicts its extratropical teleconnection for the standing, jumping, and fast-propagating MJO (averaged 11-20-day after day 0) (Fig. 11). However, the model has little skill in predicting its observed teleconnections for the slow-propagating MJO despite a useful MJO prediction skill of 31 days. It highlights the complexities and challenges of applying a skillful MJO prediction to the operational prediction of MJO impacts, such as the meteorological variables---t2m and precipitation.

8.2 Discussion

Accepted for publication in *Bulletin of the American Meteorological Society*. DOI 10.1175/BAMS-D-21-0124.1.

Why do the slow-propagating and fast-propagating MJO differ in their propagation pathway when crossing the MC: one through the southern MC and the other through the central MC (Fig. 7)? There are two possible reasons for this. First, for the fast-propagating MJO, the suppressed interannual convective variability to the south of MC may prohibit its southward pathway when crossing the MC (Fig. 8d), resulting in a rather equatorially symmetric propagation over the central MC (Fig. 7). Second, the propagation pathway can be modulated by the seasonal variation of the background mean state. Kim et al. (2017) found that the MJO preferentially detours southward near the MC during December-February (DJF), predominantly related to the meridional mean moisture gradient. Here we reveal the seasonal preference about the occurrence frequency of different types of MJO. There are more slow-propagating cases in DJF than March-April (MA) (9 vs. 3), but fewer fast-propagating MJO cases in DJF than MA (4 vs. 7) (Table 1), consistent with (Chen 2021). It also implies the MJO propagation speed may have seasonal dependence with fast (slow) propagation speed in DJF (MA). Meanwhile, there are fewer standing MJO cases in MA than DJF (Table 1). The seasonal preference indicates that the background mean state in MA tends to be more favorable for its eastward propagation of MJO than in DJF. Compared to the fast-propagating MJO, the more severe MC prediction barrier problem for the slow-propagating MJO is possibly linked to a more severe mean state bias in DJF than MA. Identifying the potential role and processes of seasonality in regulating the MJO diversity calls for deliberation. There are several other issues that are not addressed here. For example, why does the QBO have pronounced influences on the standing and slow-propagating MJO but not on the other two types of MJO (the seasonal preference of the occurrence of different MJO types may partially explain this as the connection between QBO and MJO is most prominent in DJF)? Why does the model have difficulty in predicting the teleconnections associated with the slow-propagating MJO? Whether

Accepted for publication in *Bulletin of the American Meteorological Society*. DOI 10.1175/BAMS-D-21-0124.1.

and to what extent these findings can be applied to other dynamical models is another issue calling for further studies.

Though the SPEAR model produces a comparable or even better MJO prediction skill than the majority of current operational S2S prediction models (Kim et al. 2018; Vitart 2017), there are also some caveats and limitations for the current configuration, developed for high performance computing constraints. For example, the model has a relatively coarse vertical resolution (33 levels) with a low top atmosphere. The initialization is relatively simple, and the land is not explicitly initialized, although it can be constrained by the atmospheric nudging. The system also suffers the under-dispersive issue (the ensemble spread is much smaller than the RMSE) common to many models. These caveats, however, may provide an opportunity to identify the roles of a better representation of the stratosphere and a sophisticated initialization in S2S prediction and should be explored.

Understanding and isolating skills with a global model are critical for further model development. We hope that this work provides a framework to identify potential issues for MJO prediction in individual models by examining diversified MJO, which may provide guidance for further model development. Given the different impacts from these four types of MJO, operational forecasters may need to consider more than just the RMM index when monitoring the MJO and forecasting its impacts.

The SPEAR seasonal prediction system (Delworth et al. 2020; Lu et al. 2020) is operationally participating in the North American Multi-Model Ensemble (NMME) (Kirtman et al. 2014), but was first developed for research. By developing SPEAR for S2S prediction, we have created a new system for shorter-range prediction that could similarly be used in research to further development in operational modeling. Importantly, the SPEAR model shares two key model components with

Accepted for publication in *Bulletin of the American Meteorological Society*. DOI 10.1175/BAMS-D-21-0124.1.

the Unified Forecast System (UFS) model: the Finite-Volume Cubed-Sphere (FV3) dynamical core (Lin 2004) and MOM6 ocean model (Adcroft et al. 2019). Thus, knowledge derived from the development and use of SPEAR can be used to assist in the development and application of the UFS model.

Acknowledgments

We thank the review comments from Drs Pu Lin and Kai-Chih Tseng as well as three anonymous reviewers. B. W acknowledge the support from NSF/climate dynamics award # 2025057. The ERA5 data sets are downloaded from https://cds.climate.copernicus.eu/#!/search?text=ERA5&type=dataset. The NOAA OLR data is downloaded from https://psl.noaa.gov/data/gridded/data.interp_OLR.html.

Accepted for publication in *Bulletin of the American Meteorological Society*. DOI 10.1175/BAMS-D-21-0124.1.

References

Adames, Á. F., and D. Kim, 2016: The MJO as a Dispersive, Convectively Coupled Moisture Wave: Theory and Observations. *Journal of the Atmospheric Sciences*, **73,** 913-941.

Adcroft, A., and Coauthors, 2019: The GFDL Global Ocean and Sea Ice Model OM4.0: Model Description and Simulation Features. *Journal of Advances in Modeling Earth Systems*, **11,** 3167-3211.

Benedict, J. J., and D. A. Randall, 2007: Observed Characteristics of the MJO Relative to Maximum Rainfall. *Journal of the Atmospheric Sciences*, **64,** 2332-2354.

Bladé, I., and D. L. Hartmann, 1993: Tropical Intraseasonal Oscillations in a Simple Nonlinear Model. *Journal of Atmospheric Sciences*, **50,** 2922-2939.

Bushuk, M., and Coauthors, 2021: Seasonal prediction and predictability of regional Antarctic sea ice. *Journal of Climate***,** 1-68.

Cassou, C., 2008: Intraseasonal interaction between the Madden–Julian Oscillation and the North Atlantic Oscillation. *Nature*, **455,** 523.

Chen, G., 2021: Diversity of the Global Teleconnections Associated with the Madden–Julian Oscillation. *Journal of Climate*, **34,** 397-414.

Chen, G., and B. Wang, 2020: Circulation Factors Determining the Propagation Speed of the Madden–Julian Oscillation. *Journal of Climate*, **33,** 3367-3380.

DeFlorio, M. J., D. E. Waliser, B. Guan, D. A. Lavers, F. M. Ralph, and F. Vitart, 2018: Global Assessment of Atmospheric River Prediction Skill. *Journal of Hydrometeorology*, **19,** 409-426.

Delworth, T. L., and Coauthors, 2020: SPEAR: The Next Generation GFDL Modeling System for Seasonal to Multidecadal Prediction and Projection. *Journal of Advances in Modeling Earth Systems*, **12,** e2019MS001895.

Dong, W., M. Zhao, Y. Ming, and V. Ramaswamy, 2021: Representation of Tropical Mesoscale Convective Systems in a General Circulation Model: Climatology and Response to Global Warming. *Journal of Climate***,** 1-40.

Ferranti, L., T. N. Palmer, F. Molteni, and E. Klinker, 1990: Tropical-Extratropical Interaction Associated with the 30–60 Day Oscillation and Its Impact on Medium and Extended Range Prediction. *Journal of Atmospheric Sciences*, **47,** 2177-2199.

Fu, X., J.-Y. Lee, P.-C. Hsu, H. Taniguchi, B. Wang, W. Wang, and S. Weaver, 2013: Multi-model MJO forecasting during DYNAMO/CINDY period. *Clim Dyn*, **41,** 1067-1081.

Gelaro, R., and Coauthors, 2017: The Modern-Era Retrospective Analysis for Research and Applications, Version 2 (MERRA-2). *Journal of Climate*, **30,** 5419-5454.

Haertel, P., 2021: Kelvin/Rossby Wave Partition of Madden-Julian Oscillation Circulations. *Climate*, **9**.

Harris, L., and Coauthors, 2020: GFDL SHiELD: A Unified System for Weather-to-Seasonal Prediction. *Journal of Advances in Modeling Earth Systems*, **12,** e2020MS002223.

Held, I. M., and Coauthors, 2019: Structure and Performance of GFDL's CM4.0 Climate Model. *Journal of Advances in Modeling Earth Systems*, **11,** 3691-3727.

Henderson, S. A., E. D. Maloney, and S.-W. Son, 2017: Madden–Julian Oscillation Pacific Teleconnections: The Impact of the Basic State and MJO Representation in General Circulation Models. *Journal of Climate*, **30,** 4567-4587.

Accepted for publication in *Bulletin of the American Meteorological Society*. DOI 10.1175/BAMS-D-21-0124.1.

Hsu, P.-c., and T. Li, 2012: Role of the Boundary Layer Moisture Asymmetry in Causing the Eastward Propagation of the Madden–Julian Oscillation. *Journal of Climate*, **25,** 4914-4931.

Jia, L. I. U., D. A. Yuqin, L. I. Tim, and H. U. Feng, 2020: Impact of ENSO on MJO Pattern Evolution over the Maritime Continent. *Journal of Meteorological Research*, **34,** 1151-1166.

Jiang, X., B. Xiang, M. Zhao, T. Li, S.-J. Lin, Z. Wang, and J.-H. Chen, 2018: Intraseasonal Tropical Cyclogenesis Prediction in a Global Coupled Model System. *Journal of Climate*.

Jiang, X., and Coauthors, 2020: Fifty Years of Research on the Madden-Julian Oscillation: Recent Progress, Challenges, and Perspectives. *Journal of Geophysical Research: Atmospheres*, **125,** e2019JD030911.

Kerns, B. W., and S. S. Chen, 2020: A 20-Year Climatology of Madden-Julian Oscillation Convection: Large-Scale Precipitation Tracking From TRMM-GPM Rainfall. *Journal of Geophysical Research: Atmospheres*, **125,** e2019JD032142.

Kiladis, G. N., K. H. Straub, and P. T. Haertel, 2005: Zonal and Vertical Structure of the Madden–Julian Oscillation. *Journal of the Atmospheric Sciences*, **62,** 2790-2809.

Kim, D., J.-S. Kug, and A. H. Sobel, 2014: Propagating versus Nonpropagating Madden–Julian Oscillation Events. *Journal of Climate*, **27,** 111-125.

Kim, D., H. Kim, and M.-I. Lee, 2017: Why does the MJO detour the Maritime Continent during austral summer? *Geophysical Research Letters*, **44,** 2579-2587.

Kim, H., F. Vitart, and D. E. Waliser, 2018: Prediction of the Madden–Julian Oscillation: A Review. *Journal of Climate*, **31,** 9425-9443.

Kim, H., M. A. Janiga, and K. Pegion, 2019: MJO Propagation Processes and Mean Biases in the SubX and S2S Reforecasts. *Journal of Geophysical Research: Atmospheres*, **124,** 9314-9331.

Kirtman, B. P., and Coauthors, 2014: The North American Multimodel Ensemble: Phase-1 Seasonal-to-Interannual Prediction; Phase-2 toward Developing Intraseasonal Prediction. *Bulletin of the American Meteorological Society*, **95,** 585-601.

Klotzbach, P., S. Abhik, H. H. Hendon, M. Bell, C. Lucas, A. G. Marshall, and E. C. J. Oliver, 2019: On the emerging relationship between the stratospheric Quasi-Biennial oscillation and the Madden-Julian oscillation. *Scientific Reports*, **9,** 2981.

Lee, C.-Y., S. J. Camargo, F. Vitart, A. H. Sobel, and M. K. Tippett, 2018: Subseasonal Tropical Cyclone Genesis Prediction and MJO in the S2S Dataset. *Weather and Forecasting*, **33,** 967-988.

Lee, C.-Y., and Coauthors, 2020: Subseasonal Predictions of Tropical Cyclone Occurrence and ACE in the S2S Dataset. *Weather and Forecasting*, **35,** 921-938.

Li, T., L. Wang, M. Peng, B. Wang, C. Zhang, W. Lau, and H.-C. Kuo, 2018: A Paper on the Tropical Intraseasonal Oscillation Published in 1963 in a Chinese Journal. *Bulletin of the American Meteorological Society*, **99,** 1765-1779.

Liebmann, B., and C. A. Smith, 1996: Description of a Complete (Interpolated) Outgoing Longwave Radiation Dataset. *Bulletin of the American Meteorological Society*, **77,** 1275-1277.

Lim, Y., S.-W. Son, and D. Kim, 2018: MJO Prediction Skill of the Subseasonal-to-Seasonal Prediction Models. *Journal of Climate*, **31,** 4075-4094.

Lim, Y., S.-W. Son, A. G. Marshall, H. H. Hendon, and K.-H. Seo, 2019: Influence of the QBO on MJO prediction skill in the subseasonal-to-seasonal prediction models. *Clim Dyn*, **53,** 1681-1695.

Lin, H., G. Brunet, and J. Derome, 2008: Forecast Skill of the Madden–Julian Oscillation in Two Canadian Atmospheric Models. *Monthly Weather Review*, **136,** 4130-4149.

Accepted for publication in *Bulletin of the American Meteorological Society*. DOI 10.1175/BAMS-D-21-0124.1.

——, 2009: An Observed Connection between the North Atlantic Oscillation and the Madden–Julian Oscillation. *Journal of Climate*, **22,** 364-380.

Lin, H., G. Brunet, and S. Fontecilla Juan, 2010: Impact of the Madden-Julian Oscillation on the intraseasonal forecast skill of the North Atlantic Oscillation. *Geophysical Research Letters*, **37**.

Lin, S.-J., 2004: A "Vertically Lagrangian" Finite-Volume Dynamical Core for Global Models. *Monthly Weather Review*, **132,** 2293-2307.

Liu, C., B. Tian, K.-F. Li, G. L. Manney, N. J. Livesey, Y. L. Yung, and D. E. Waliser, 2014: Northern Hemisphere mid-winter vortex-displacement and vortex-split stratospheric sudden warmings: Influence of the Madden-Julian Oscillation and Quasi-Biennial Oscillation. *Journal of Geophysical Research: Atmospheres*, **119,** 12,599-512,620.

Lu, F., and Coauthors, 2020: GFDL's SPEAR seasonal prediction system: initialization and ocean tendency adjustment (OTA) for coupled model predictions. *Journal of Advances in Modeling Earth Systems*, **n/a,** e2020MS002149.

Lyu, M., X. Jiang, Z. Wu, D. Kim, and Á. F. Adames, 2021: Zonal-Scale of the Madden-Julian Oscillation and Its Propagation Speed on the Interannual Time-Scale. *Geophysical Research Letters*, **48,** e2020GL091239.

Madden, R. A., and P. R. Julian, 1971: Detection of a 40–50 Day Oscillation in the Zonal Wind in the Tropical Pacific. *Journal of Atmospheric Sciences*, **28,** 702-708.

——, 1972: Description of Global-Scale Circulation Cells in the Tropics with a 40–50 Day Period. *Journal of Atmospheric Sciences*, **29,** 1109-1123.

Marshall, A. G., H. H. Hendon, S.-W. Son, and Y. Lim, 2017: Impact of the quasi-biennial oscillation on predictability of the Madden–Julian oscillation. *Clim Dyn*, **49,** 1365-1377.

Martin, Z., and Coauthors, 2021: The influence of the quasi-biennial oscillation on the Madden–Julian oscillation. *Nature Reviews Earth & Environment*, **2,** 477-489.

Matthews, A. J., 2008: Primary and successive events in the Madden–Julian Oscillation. *Quarterly Journal of the Royal Meteorological Society*, **134,** 439-453.

Mundhenk, B. D., E. A. Barnes, E. D. Maloney, and C. F. Baggett, 2018: Skillful empirical subseasonal prediction of landfalling atmospheric river activity using the Madden–Julian oscillation and quasi-biennial oscillation. *npj Climate and Atmospheric Science*, **1,** 20177.

Murakami, H., T. L. Delworth, W. F. Cooke, M. Zhao, B. Xiang, and P.-C. Hsu, 2020: Detected climatic change in global distribution of tropical cyclones. *Proceedings of the National Academy of Sciences*, **117,** 10706.

Nardi, K. M., C. F. Baggett, E. A. Barnes, E. D. Maloney, D. S. Harnos, and L. M. Ciasto, 2020: Skillful All-Season S2S Prediction of U.S. Precipitation Using the MJO and QBO. *Weather and Forecasting*, **35,** 2179-2198.

Neena, J. M., J. Y. Lee, D. Waliser, B. Wang, and X. Jiang, 2014: Predictability of the Madden–Julian Oscillation in the Intraseasonal Variability Hindcast Experiment (ISVHE). *Journal of Climate*, **27,** 4531-4543.

Rashid, H. A., H. H. Hendon, M. C. Wheeler, and O. Alves, 2011: Prediction of the Madden–Julian oscillation with the POAMA dynamical prediction system. *Clim Dyn*, **36,** 649-661.

Ren, H.-L., J. Wu, C.-B. Zhao, Y.-J. Cheng, and X.-W. Liu, 2016: MJO ensemble prediction in BCC-CSM1.1(m) using different initialization schemes. *Atmospheric and Oceanic Science Letters*, **9,** 60-65.

Accepted for publication in *Bulletin of the American Meteorological Society*. DOI 10.1175/BAMS-D-21-0124.1.

Reynolds, R. W., T. M. Smith, C. Liu, D. B. Chelton, K. S. Casey, and M. G. Schlax, 2007: Daily High-Resolution-Blended Analyses for Sea Surface Temperature. *Journal of Climate*, **20,** 5473-5496.

Rogers, J. C., 1981: The North Pacific Oscillation. *Journal of Climatology*, **1,** 39-57.

Stan, C., D. M. Straus, J. S. Frederiksen, H. Lin, E. D. Maloney, and C. Schumacher, 2017: Review of Tropical-Extratropical Teleconnections on Intraseasonal Time Scales. *Reviews of Geophysics*, **55,** 902-937.

Tseng, K.-C., E. Maloney, and E. Barnes, 2019: The Consistency of MJO Teleconnection Patterns: An Explanation Using Linear Rossby Wave Theory. *Journal of Climate*, **32,** 531-548.

Vitart, F., 2009: Impact of the Madden Julian Oscillation on tropical storms and risk of landfall in the ECMWF forecast system. *Geophysical Research Letters*, **36**.

Vitart, F., 2017: Madden—Julian Oscillation prediction and teleconnections in the S2S database. *Quarterly Journal of the Royal Meteorological Society*, **143,** 2210-2220.

Wang, B., 1988: Dynamics of Tropical Low-Frequency Waves: An Analysis of the Moist Kelvin Wave. *Journal of Atmospheric Sciences*, **45,** 2051-2065.

Wang, B., and H. Rui, 1990: Synoptic climatology of transient tropical intraseasonal convection anomalies: 1975–1985. *Meteorology and Atmospheric Physics*, **44,** 43-61.

Wang, B., and S.-S. Lee, 2017: MJO Propagation Shaped by Zonal Asymmetric Structures: Results from 24 GCM Simulations. *Journal of Climate*, **30,** 7933-7952.

Wang, B., F. Liu, and G. Chen, 2016: A trio-interaction theory for Madden–Julian oscillation. *Geoscience Letters*, **3,** 34.

Wang, B., G. Chen, and F. Liu, 2019a: Diversity of the Madden-Julian Oscillation. *Science Advances*, **5,** eaax0220.

Wang, J., H. Kim, D. Kim, S. A. Henderson, C. Stan, and E. D. Maloney, 2020: MJO Teleconnections over the PNA Region in Climate Models. Part II: Impacts of the MJO and Basic State. *Journal of Climate*, **33,** 5081-5101.

Wang, S., M. K. Tippett, A. H. Sobel, Z. K. Martin, and F. Vitart, 2019b: Impact of the QBO on Prediction and Predictability of the MJO Convection. *Journal of Geophysical Research: Atmospheres*, **124,** 11766-11782.

Weaver, S. J., W. Wang, M. Chen, and A. Kumar, 2011: Representation of MJO Variability in the NCEP Climate Forecast System. *Journal of Climate*, **24,** 4676-4694.

Wei, Y., and H.-L. Ren, 2019: Modulation of ENSO on Fast and Slow MJO Modes during Boreal Winter. *Journal of Climate*, **32,** 7483-7506.

Wheeler, M. C., and H. H. Hendon, 2004: An All-Season Real-Time Multivariate MJO Index: Development of an Index for Monitoring and Prediction. *Monthly Weather Review*, **132,** 1917-1932.

Wu, J., H.-L. Ren, B. Lu, P. Zhang, C. Zhao, and X. Liu, 2020: Effects of Moisture Initialization on MJO and its Teleconnection Prediction in BCC Subseasonal Coupled Model. *Journal of Geophysical Research: Atmospheres*, **125,** e2019JD031537.

Xiang, B., Y. Q. Sun, J.-H. Chen, N. C. Johnson, and X. Jiang, 2020: Subseasonal Prediction of Land Cold Extremes in Boreal Wintertime. *Journal of Geophysical Research: Atmospheres*, **125,** e2020JD032670.

Xiang, B., M. Zhao, X. Jiang, S.-J. Lin, T. Li, X. Fu, and G. Vecchi, 2015: The 3–4-Week MJO Prediction Skill in a GFDL Coupled Model. *Journal of Climate*, **28,** 5351-5364.

Accepted for publication in *Bulletin of the American Meteorological Society*. DOI 10.1175/BAMS-D-21-0124.1.

Xiang, B., and Coauthors, 2014: Beyond Weather Time-Scale Prediction for Hurricane Sandy and Super Typhoon Haiyan in a Global Climate Model. *Monthly Weather Review*, **143,** 524-535.

Yoo, C., and S.-W. Son, 2016: Modulation of the boreal wintertime Madden-Julian oscillation by the stratospheric quasi-biennial oscillation. *Geophysical Research Letters*, **43,** 1392-1398.

Zhang, C., and B. Zhang, 2018: QBO-MJO Connection. *Journal of Geophysical Research: Atmospheres*, **123,** 2957-2967.

Zhang, C., Á. F. Adames, B. Khouider, B. Wang, and D. Yang, 2020: Four Theories of the Madden-Julian Oscillation. *Reviews of Geophysics*, **58,** e2019RG000685.

Zhao, M., 2020: Simulations of Atmospheric Rivers, Their Variability, and Response to Global Warming Using GFDL's New High-Resolution General Circulation Model. *Journal of Climate*, **33,** 10287-10303.

Zhao, M., and Coauthors, 2018a: The GFDL Global Atmosphere and Land Model AM4.0/LM4.0: 1. Simulation Characteristics With Prescribed SSTs. *Journal of Advances in Modeling Earth Systems*, **10,** 691-734.

Zhao, M., and Coauthors, 2018b: The GFDL Global Atmosphere and Land Model AM4.0/LM4.0: 2. Model Description, Sensitivity Studies, and Tuning Strategies. *Journal of Advances in Modeling Earth Systems*, **10,** 735-769.

Zhu, J., and A. Kumar, 2019: Role of Sea Surface Salinity Feedback in MJO Predictability: A Study with CFSv2. *Journal of Climate*, **32,** 5745-5759.

Zhu, J., A. Kumar, and W. Wang, 2020: Dependence of MJO Predictability on Convective Parameterizations. *Journal of Climate*, **33,** 4739-4750.

Accepted for publication in *Bulletin of the American Meteorological Society*. DOI 10.1175/BAMS-D-21-0124.1.

Table and Figure captions

Table 1 The temporal midpoint of the selected four clusters of the observed MJO events. Each MJO case is defined when the area-averaged OLR anomalies in the equatorial Indian Ocean (75°E-95°E, 10°S-10°N) are below one standard deviation for five successive days. The total number of events is shown in the first row in the parentheses.

Figure 1 MJO prediction skill during boreal wintertime (November to April) from 2000 to 2019 made by the GFDL SPEAR model. a) The bivariate anomalous correlation coefficient (ACC) measured by the RMM index from individual members (grey) and ten-member ensemble mean (red). b) the RMM index root mean square error (RMSE) from individual members (grey) and their ensemble mean (red). The blue line denotes the ensemble spread relative to the ten-member ensemble mean.

Figure 2 a) The bivariate ACC for initially strong (red) and initially weak (black) MJO cases. b) The ACC as a function of initial phases (x-axis) and forecast lead days (y-axis). c) The bivariate ACC for target strong (red) and target weak (black) MJO cases as a function of forecast lag days. d) The ACC as a function of target phases and forecast lag days. “Strong MJO” (Weak MJO) is defined as all days with |RMM|>1 (|RMM|<1).

Figure 3 Prediction skill for MJO amplitude and phase angle. a) The time evolution of MJO amplitude as a function of forecast lead days for initially strong cases from observations (black) and model prediction from the ensemble mean (solid red) and mean of individual members (dashed

Accepted for publication in *Bulletin of the American Meteorological Society*. DOI 10.1175/BAMS-D-21-0124.1.

red). b) The observed (black bars) and predicted (red bars) MJO amplitude averaged over the first 25 days for initially strong cases as a function of eight different MJO phases (*x*-axis). c) Prediction of MJO phase angle error (°) as a function of forecast lead time for the initially strong cases. d) The predicted MJO phase error averaged over the first 25 days for initially strong cases as a function of eight different MJO phases (*x*-axis).

Figure 4 Four types of MJO events and their prediction skills in the SPEAR model. a) The ACC and b) potential predictability for four clusters of MJO. c) -f) Longitude (x-axis)-time (y-axis) composite of equatorial (10°S-10°N) OLR anomalies (W/m^2) for four types of MJO centered at day 0 when the domain-averaged OLR anomalies in the equatorial Indian Ocean (10°S-10°N, 75°E-95°E) are below one standard deviation for five successive days.

Figure 5 Prediction skill dependence of MJO diversity on the initial amplitude. a) The ACC for four types of MJO initiated at strong (|RMM|>1; solid) and weak (|RMM|<1; dash) cases. b) the observed MJO amplitude ($\sqrt{RMM1^2 + RMM2^2}$) for four groups of MJO as a function of forecast lead days (x-axis) by counting all the selected cases (initiated between 20 days before and 15 days after day 0). There are 42, 59, 85, 67 initially strong cases and 46, 45, 31, 25 initially weak cases for these four types of MJO.

Figure 6 MJO propagation and proposed mechanisms seen from the equatorial (10°S-10°N) anomalies as a function of longitude (x-axis) and time lag (y-axis; days) composited for four types of MJO. The first row: observed OLR anomalies (shading; W/m^2) and 850 hPa zonal winds (contours with an interval of 0.6 m/s). The second row: observed lower-tropospheric divergence

Accepted for publication in *Bulletin of the American Meteorological Society*. DOI 10.1175/BAMS-D-21-0124.1.

(shading; 10^{-6} S^{-1}) averaged over two levels (850 hPa and 925 hPa) and specific humidity (contours with an interval of 0.2 g/kg) averaged over two levels (700 hPa and 825 hPa). The bottom two rows are similar to the top two but for model predictions initiated at day -5 (5 days before the peak phase in the Indian Ocean). The black stippling denotes the regions at the 10% significance level.

Figure 7 Comparison of observed and predicted anomalies during the first four weeks initiated at day -5. The observed composite anomalies of OLR (W/m^2), 850 hPa winds (m/s, not shown when wind speed is less than 0.5 m/s), and 850 hPa geopotential height (contours; m^2/s^2) during the first (the first row), the second (the second row), the third (the third row), and the fourth (fourth row) weeks starting from day -5. The bottoms four rows are similar to the top four but for model predictions initiated at day -5. The MJO type is indicated at the top of each column. The black stippling denotes the regions at the 10% significance level for OLR anomalies.

Figure 8 Regulation of ENSO and stratospheric QBO on MJO diversity. Left panel: The observed interannual SST (°C; shading) and OLR anomalies (W/ m^2; contours) between day -15 and day +15. Right panel: The observed interannual 50 hPa zonal wind anomalies (m/s) between day -15 and day +15. The MJO type is indicated at the left of each row. The black stippling denotes the regions at the 10% significance level for SST anomalies (left panel) and 50 hPa zonal wind anomalies (right panel). Note that all cases initialized from November to April are used here.

Figure 9 Model's skill in predicting the target peak phase in the equatorial Indian Ocean (at around day 0) with different lead times for the four types of MJO. First row: the observed composite anomalies of OLR (shading; W/m^2) and 850 hPa winds (m/s, not shown when wind speed is less

Accepted for publication in *Bulletin of the American Meteorological Society*. DOI 10.1175/BAMS-D-21-0124.1.

than 0.5 m/s) averaged over days 1 to 5 for the four MJO clusters. The second to fifth rows are the composite results from model predictions with a lead time of 5 to 20 days, respectively. The black stippling denotes the regions with significant composite anomalies at the 10% significance level.

Figure 10 Observed precursors for the four types of MJO. First row: the observed composite anomalies of OLR (shading; W/m^2) and 850 hPa winds (m/s, not shown when wind speed is less than 0.5 m/s) averaged over the period between day -5 and day -1 for four MJO clusters. The second to fourth rows are similar but for 10, 15, and 20 days before the peak phase. The bottom four rows are similar but for the time evolutions of forecast initiated at day -20. The black stippling denotes the regions with significant OLR composite anomalies at the 10% significance level. Green boxes in the lowest panels for both observations and model forecast denote the key regions with precursory OLR signals.

Figure 11 Observed and predicted teleconnection patterns associated with the four types of MJO. a-d) The composite observational anomalies of 2m temperature (shading; °C) and 500 hPa geopotential height (contours; m^2/s^2) averaged over 11 to 20 days after the peak phase (between day 11 and 20) for the four types of MJO, e-h) Similar to a-d) but for model predictions initiated at peak phase (around day 0). The correlation skills of 2m temperature anomalies are shown in parentheses.

Accepted for publication in *Bulletin of the American Meteorological Society*. DOI 10.1175/BAMS-D-21-0124.1.

Table and Figures

Table 1 The temporal midpoint of the selected four clusters of the observed MJO events. Each MJO case is defined when the area-averaged OLR anomalies in the equatorial Indian Ocean (75°E-95°E, 10°S-10°N) are below one standard deviation for five successive days. The total number of events is shown in the first row in the parentheses.

Standing (12)	**Jumping (14)**	**Slow-propagating (15)**	**Fast-propagating (13)**
2003-01-31	2002-01-22	2000-11-18	2002-04-30
2003-11-09	2002-03-21	2001-01-27	2002-11-13
2005-02-18	2004-11-01	2001-11-18	2003-12-09
2008-11-16	2005-01-04	2002-12-23	2005-03-29
2010-11-25	2005-12-12	2006-01-11	2006-12-25
2011-02-03	2006-04-23	2006-03-19	2009-04-09
2011-11-27	2010-03-27	2007-12-13	2012-03-09
2011-12-21	2011-04-30	2008-01-28	2012-11-05
2012-04-21	2012-01-27	2009-11-10	2012-12-27
2017-01-01	2016-02-06	2009-12-30	2018-04-18
2017-02-26	2016-03-15	2010-02-12	2019-01-19
2017-04-12	2017-11-28	2013-02-08	2019-03-03
	2018-01-20	2013-03-31	2019-04-23
	2018-03-05	2015-02-11	
		2015-04-05	

Accepted for publication in *Bulletin of the American Meteorological Society*. DOI 10.1175/BAMS-D-21-0124.1.

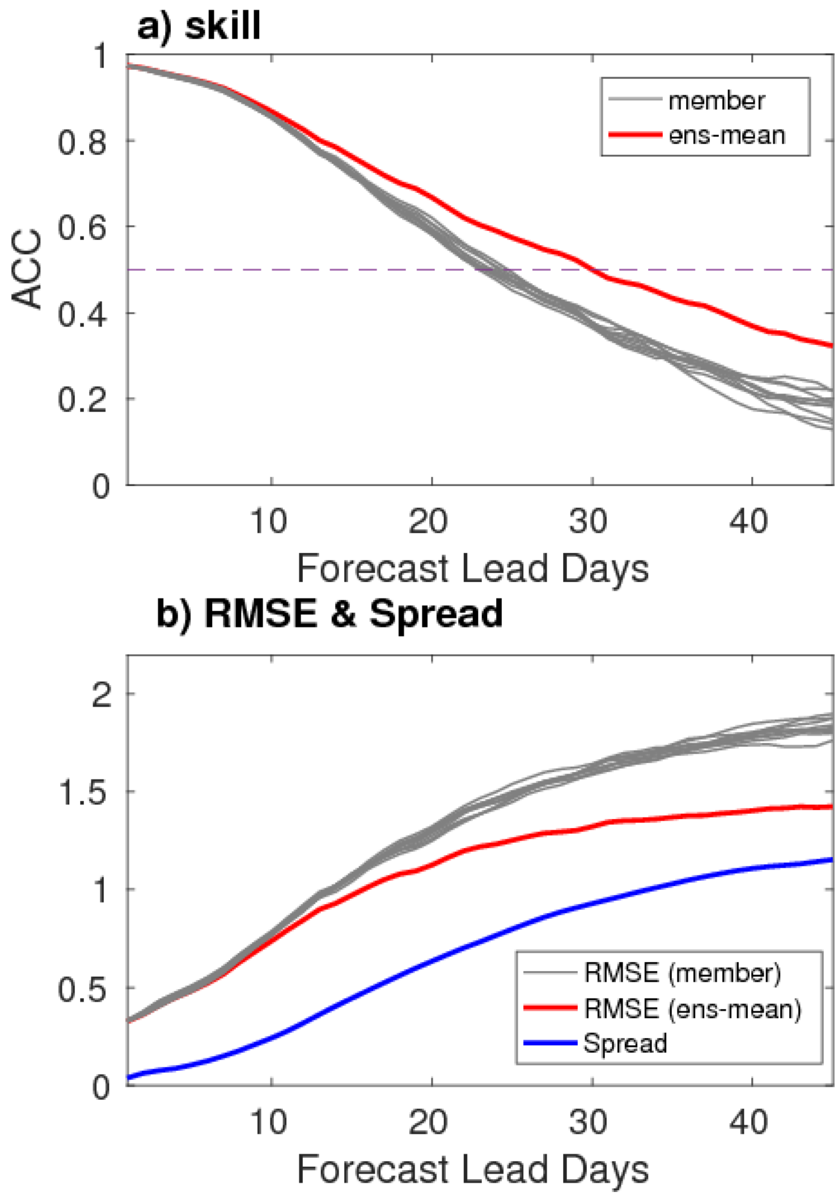

Figure 1 MJO prediction skill during boreal wintertime (November to April) from 2000 to 2019 made by the GFDL SPEAR model. a) The bivariate anomalous correlation coefficient (ACC) measured by the RMM index from individual members (grey) and ten-member ensemble mean (red). b) the RMM index root mean square error (RMSE) from individual members (grey) and their ensemble mean (red). The blue line denotes the ensemble spread relative to the ten-member ensemble mean.

Accepted for publication in *Bulletin of the American Meteorological Society*. DOI 10.1175/BAMS-D-21-0124.1.

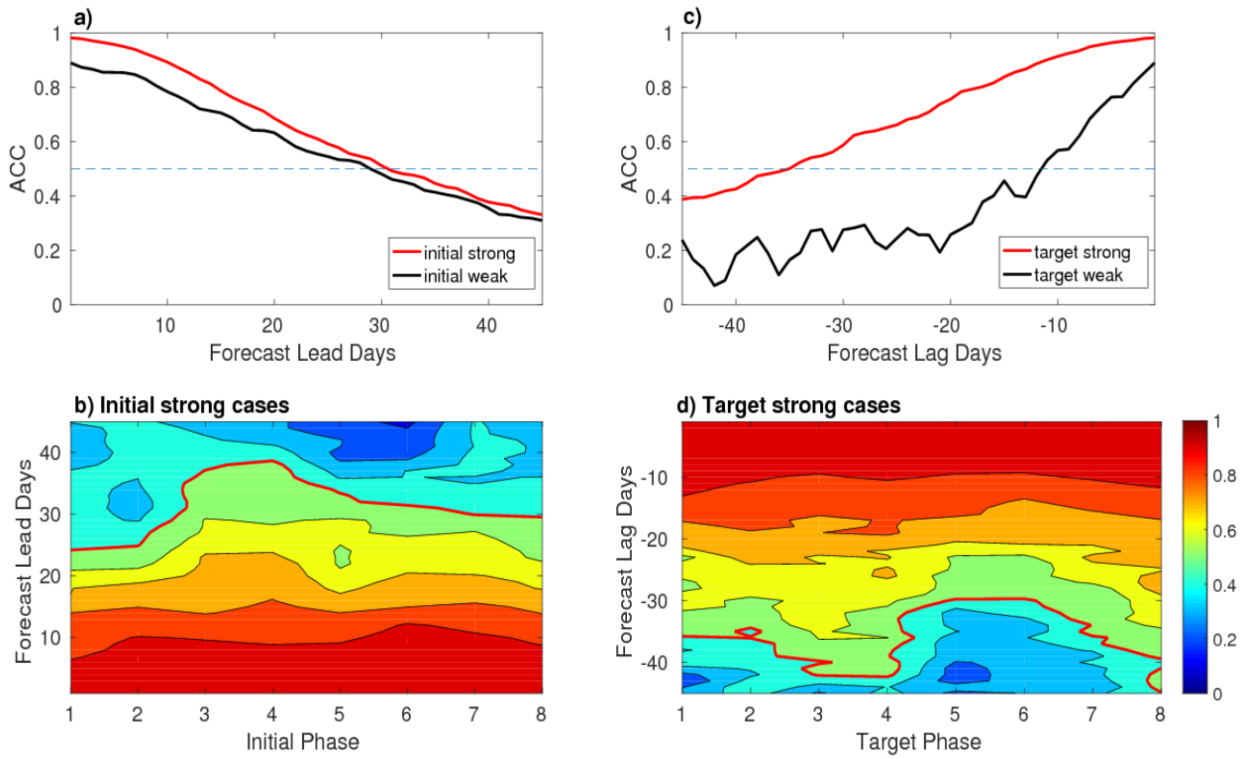

Figure 2 a) The bivariate ACC for initially strong (red) and initially weak (black) MJO cases. b) The ACC as a function of initial phases (x-axis) and forecast lead days (y-axis). c) The bivariate ACC for target strong (red) and target weak (black) MJO cases as a function of forecast lag days. d) The ACC as a function of target phases and forecast lag days. "Strong MJO" (Weak MJO) is defined as all days with |RMM|>1 (|RMM|<1).

Accepted for publication in *Bulletin of the American Meteorological Society*. DOI 10.1175/BAMS-D-21-0124.1.

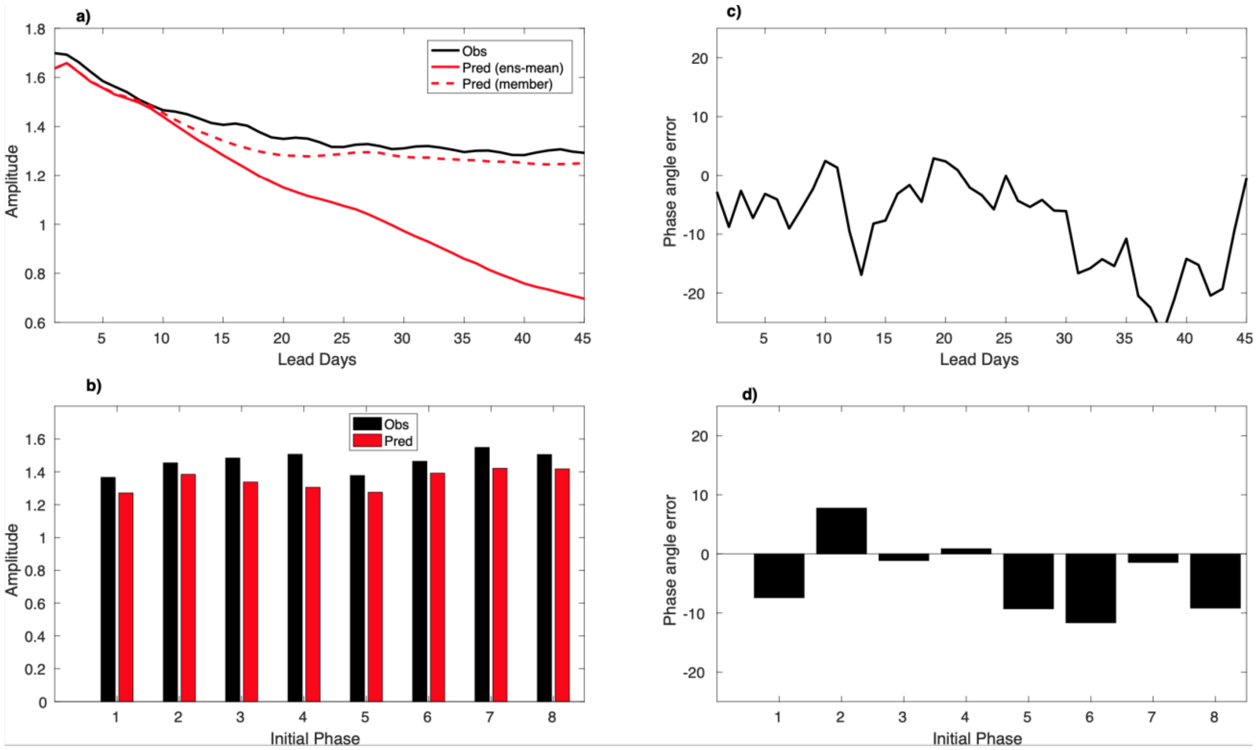

Figure 3 Prediction skill for MJO amplitude and phase angle. a) The time evolution of MJO amplitude as a function of forecast lead days for initially strong cases from observations (black) and model prediction from the ensemble mean (solid red) and mean of individual members (dashed red). b) The observed (black bars) and predicted (red bars) MJO amplitude averaged over the first 25 days for initially strong cases as a function of eight different MJO phases (*x*-axis). c) Prediction of MJO phase angle error (°) as a function of forecast lead time for the initially strong cases. d) The predicted MJO phase error averaged over the first 25 days for initially strong cases as a function of eight different MJO phases (*x*-axis).

Accepted for publication in *Bulletin of the American Meteorological Society*. DOI 10.1175/BAMS-D-21-0124.1.

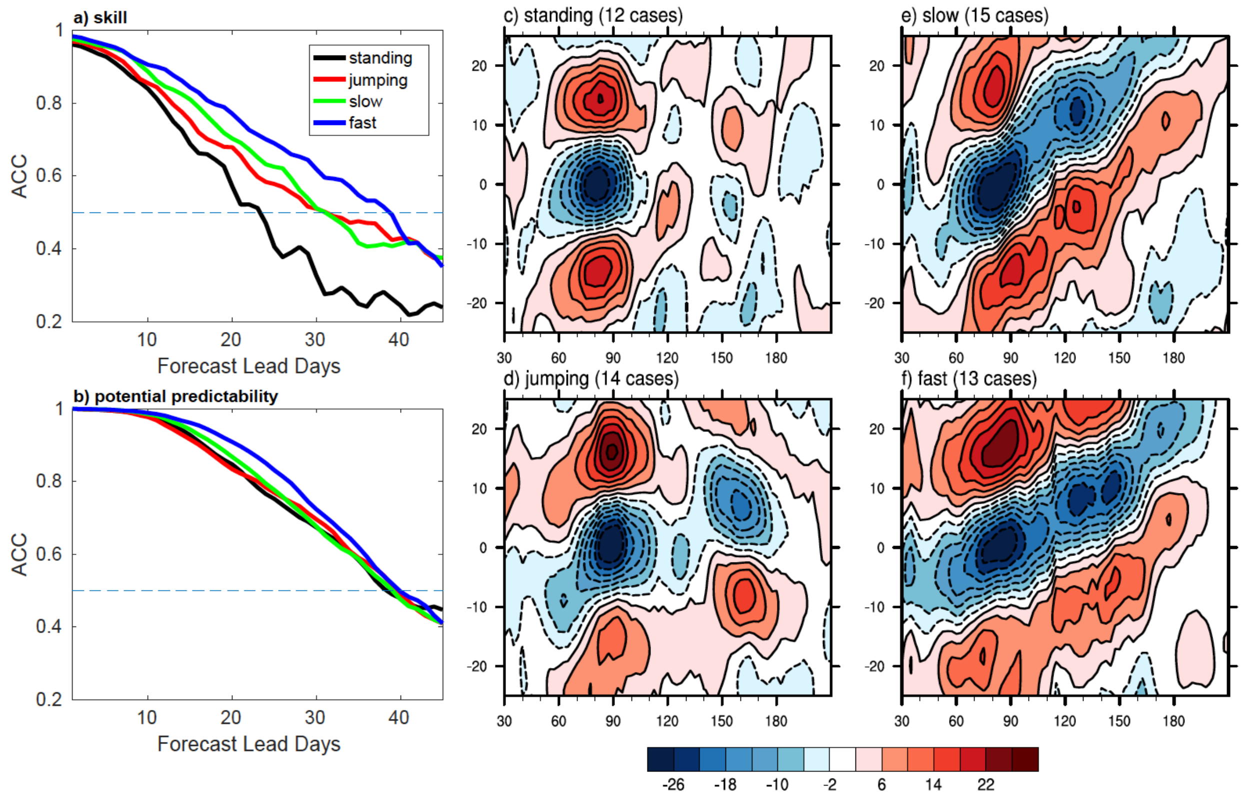

Figure 4 Four types of MJO events and their prediction skills in the SPEAR model. a) The ACC and b) potential predictability for four clusters of MJO. c) -f) Longitude (x-axis)-time (y-axis) composite of equatorial (10°S-10°N) OLR anomalies (W/m^2) for four types of MJO centered at day 0 when the domain-averaged OLR anomalies in the equatorial Indian Ocean (10°S-10°N, 75°E-95°E) are below one standard deviation for five successive days.

Accepted for publication in *Bulletin of the American Meteorological Society*. DOI 10.1175/BAMS-D-21-0124.1.

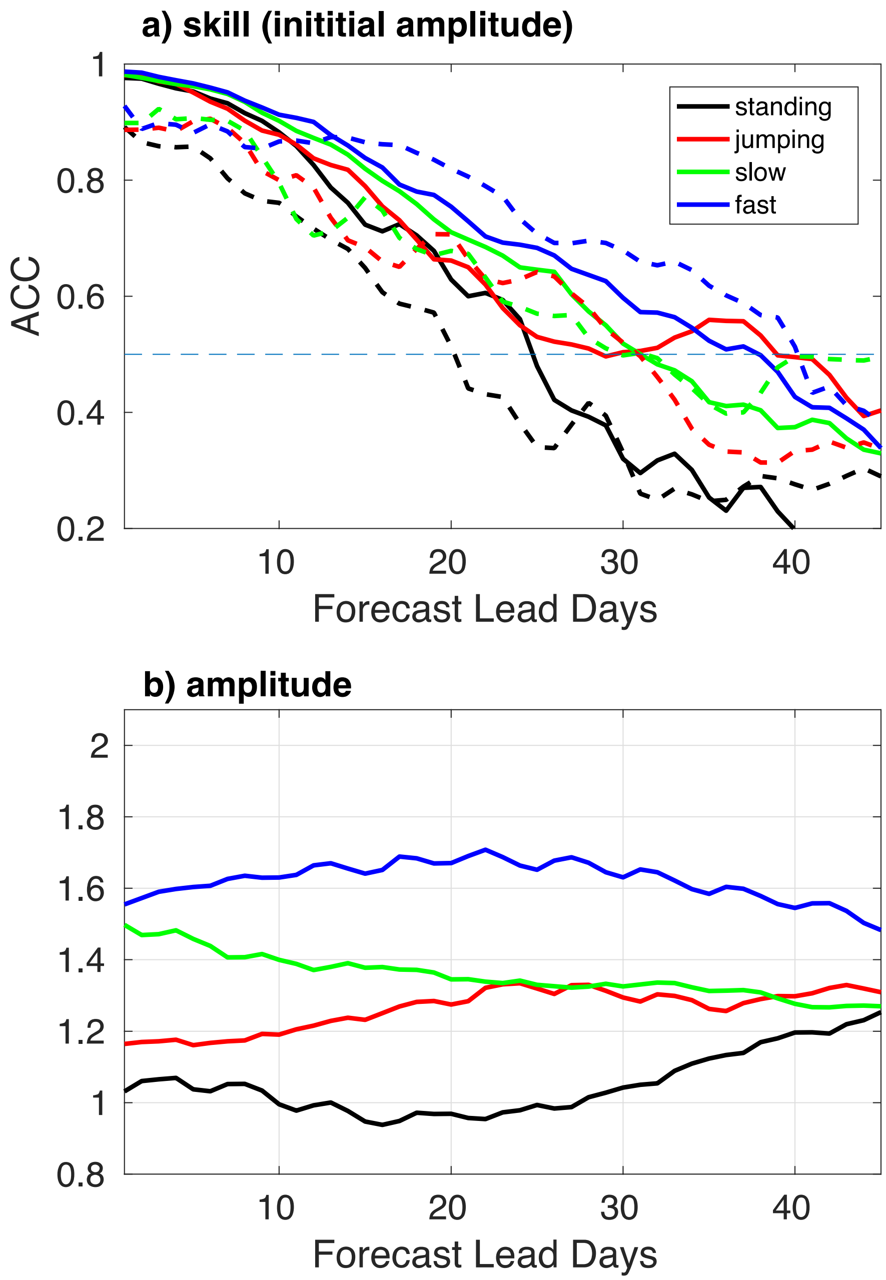

Figure 5 Prediction skill dependence of MJO diversity on the initial amplitude. a) The ACC for four types of MJO initiated at strong (|RMM|>1; solid) and weak (|RMM|<1; dash) cases. b) the observed MJO amplitude ($\sqrt{RMM1^2 + RMM2^2}$) for four groups of MJO as a function of forecast lead days (x-axis) by counting all the selected cases (initiated between 20 days before and 15 days after day 0). There are 42, 59, 85, 67 initially strong cases and 46, 45, 31, 25 initially weak cases for these four types of MJO.

Accepted for publication in *Bulletin of the American Meteorological Society*. DOI 10.1175/BAMS-D-21-0124.1.

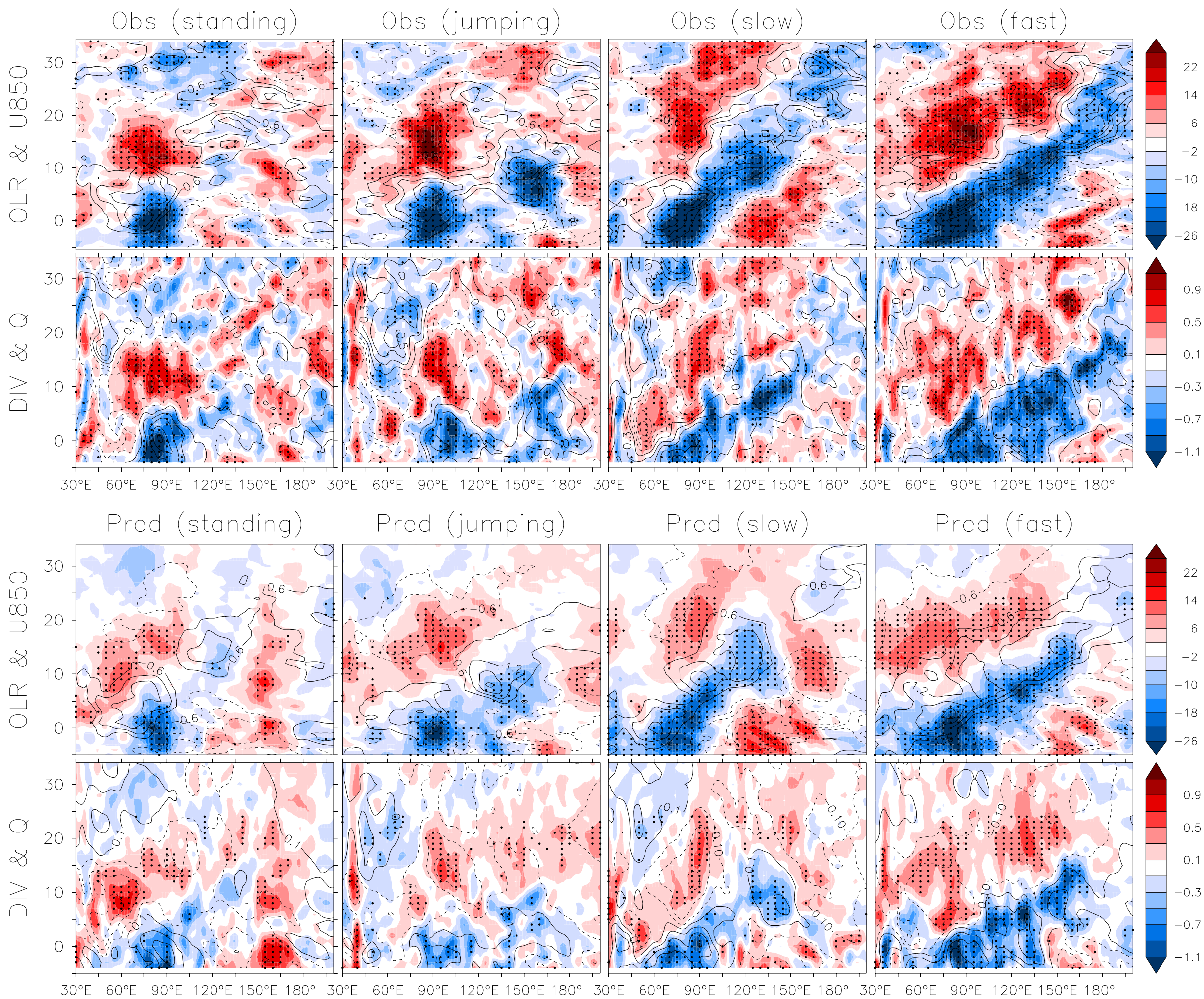

Figure 6 MJO propagation and proposed mechanisms seen from the equatorial (10°S-10°N) anomalies as a function of longitude (x-axis) and time lag (y-axis; days) composited for four types of MJO. The first row: observed OLR anomalies (shading; W/m^2) and 850 hPa zonal winds (contours with an interval of 0.6 m/s). The second row: observed lower-tropospheric divergence (shading; 10^{-6} S^{-1}) averaged over two levels (850 hPa and 925 hPa) and specific humidity (contours with an interval of 0.2 g/kg) averaged over two levels (700 hPa and 825 hPa). The bottom two rows are similar to the top two but for model predictions initiated at day -5 (5 days before the peak phase in the Indian Ocean). The black stippling denotes the regions at the 10% significance level.

Accepted for publication in *Bulletin of the American Meteorological Society*. DOI 10.1175/BAMS-D-21-0124.1.

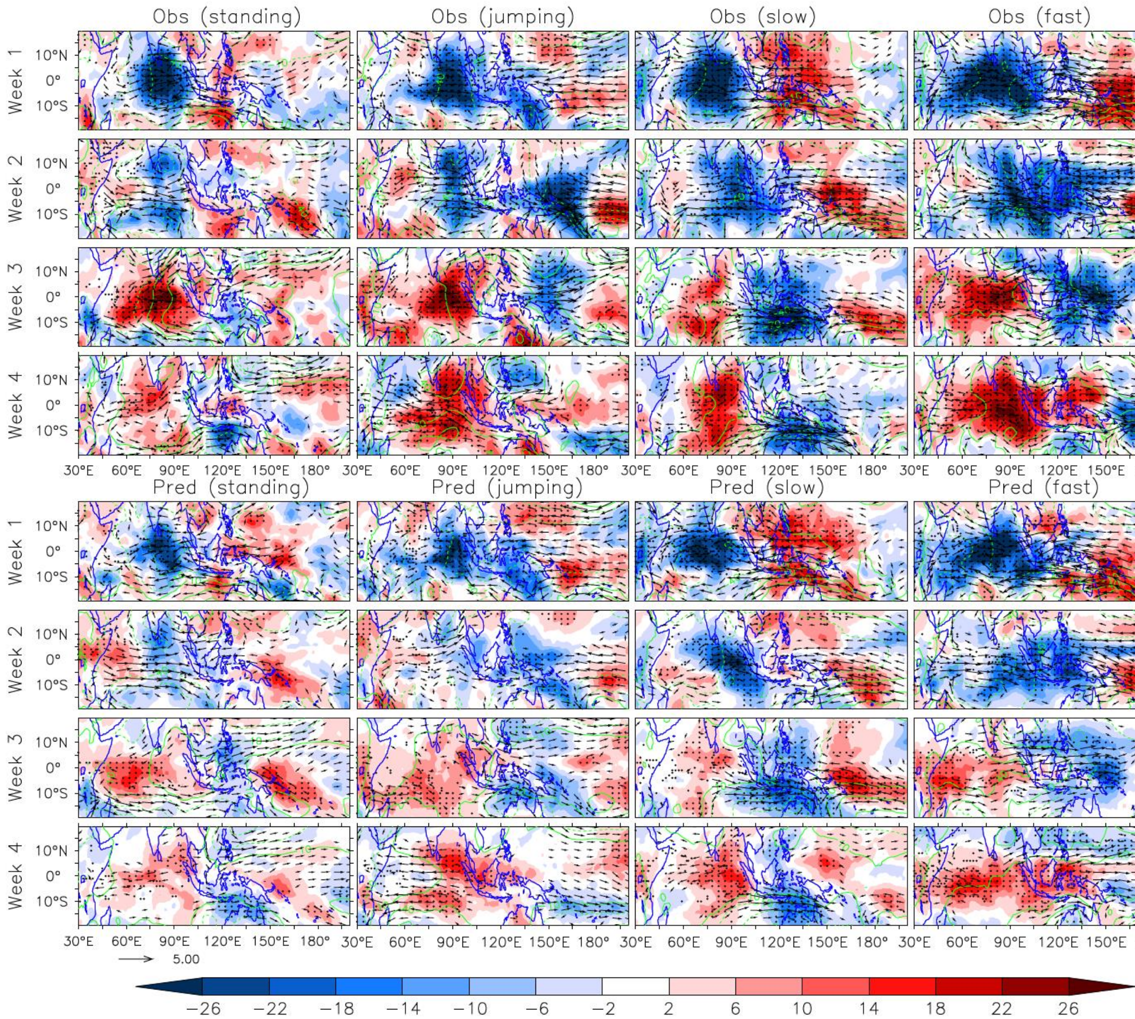

Figure 7 Comparison of observed and predicted anomalies during the first four weeks initiated at day -5. The observed composite anomalies of OLR (W/m^2), 850 hPa winds (m/s, not shown when wind speed is less than 0.5 m/s) and 850 hPa geopotential height (contours; m^2/s^2) during the first (the first row), the second (the second row), the third (the third row), and the fourth (fourth row) weeks starting from day -5. The bottoms four rows are similar to the top four but for model predictions initiated at day -5. The MJO type is indicated at the top of each column. The black stippling denotes the regions at the 10% significance level for OLR anomalies.

Accepted for publication in *Bulletin of the American Meteorological Society*. DOI 10.1175/BAMS-D-21-0124.1.

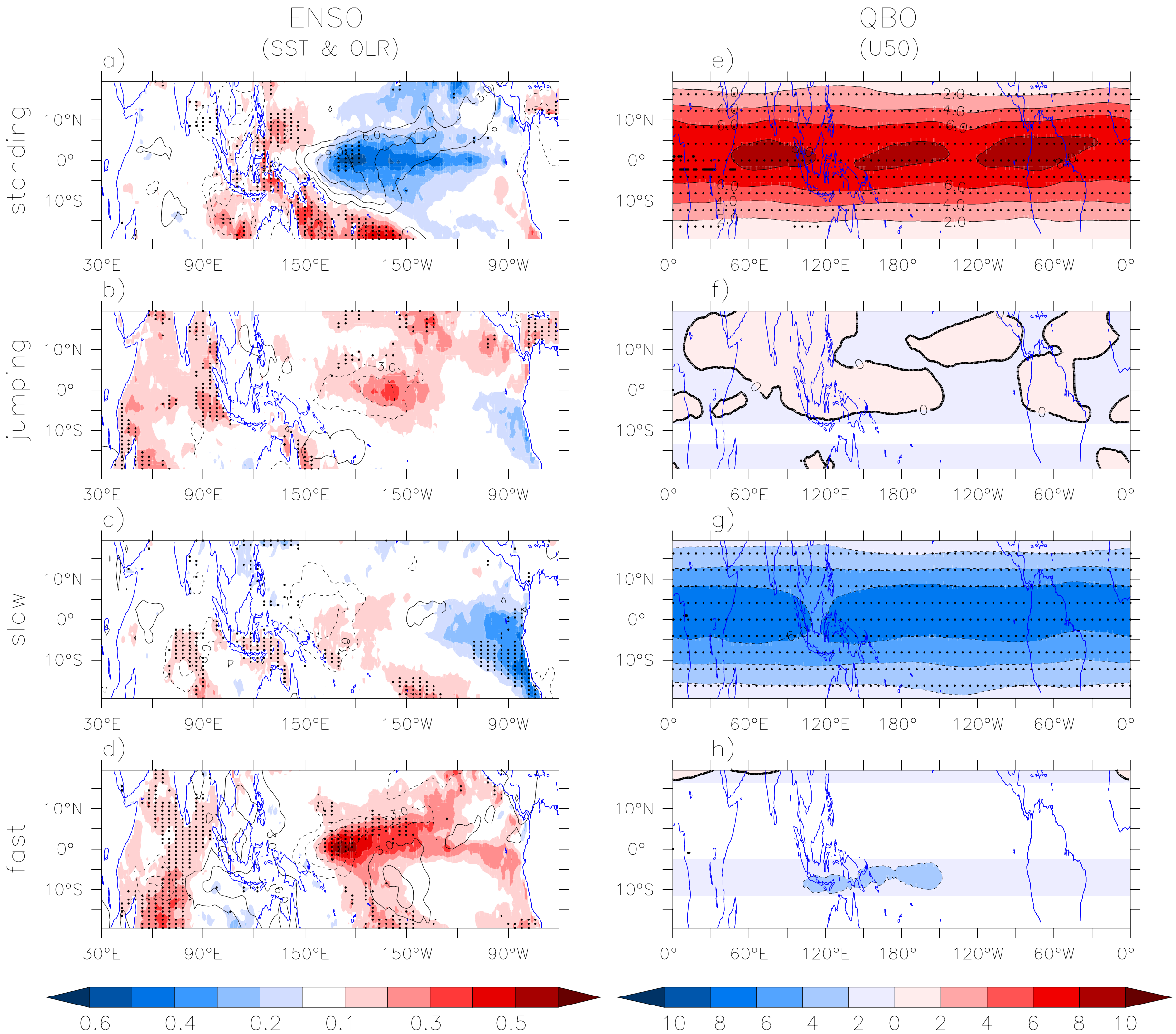

Figure 8 Regulation of ENSO and stratospheric QBO on MJO diversity. Left panel: The observed interannual SST (°C; shading) and OLR anomalies (W/ m^2; contours) between day -15 and day +15. Right panel: The observed interannual 50 hPa zonal wind anomalies (m/s) between day -15 and day +15. The MJO type is indicated at the left of each row. The black stippling denotes the regions at the 10% significance level for SST anomalies (left panel) and 50 hPa zonal wind anomalies (right panel). Note that all cases initialized from November to April are used here.

Accepted for publication in *Bulletin of the American Meteorological Society*. DOI 10.1175/BAMS-D-21-0124.1.

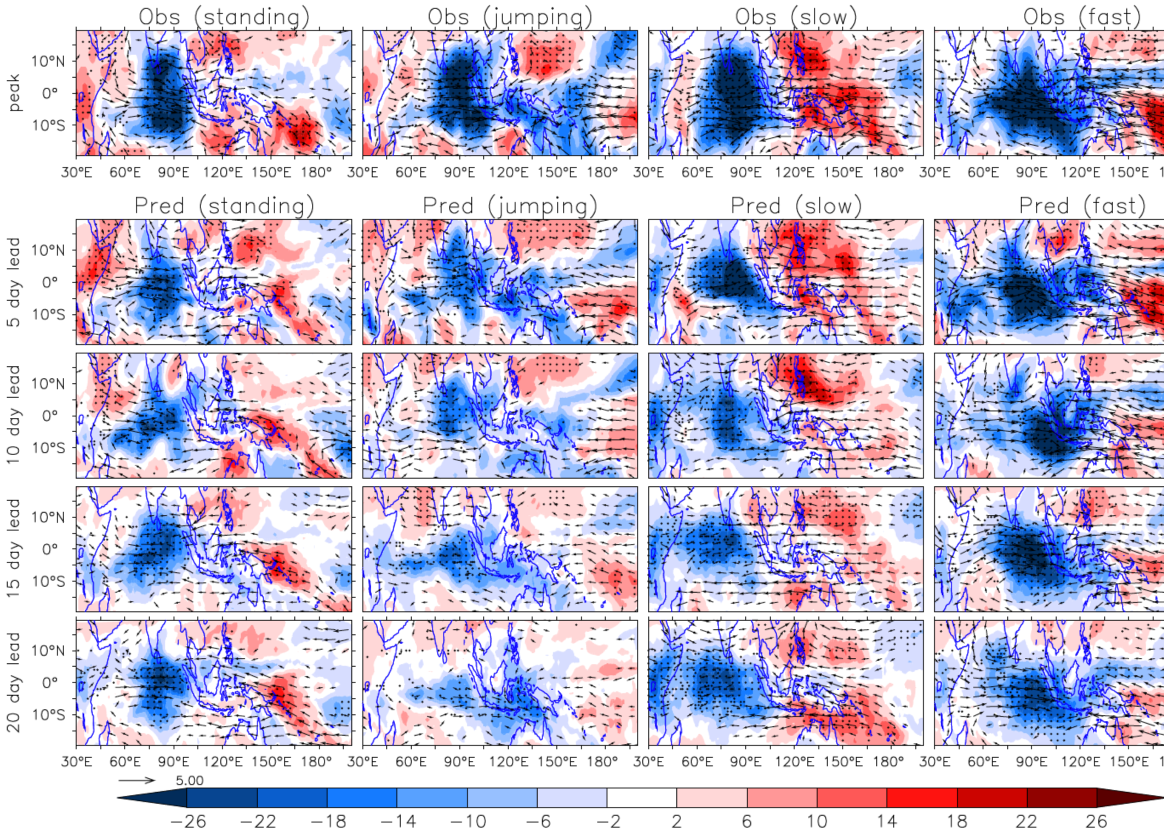

Figure 9 Model's skill in predicting the target peak phase in the equatorial Indian Ocean (at around day 0) with different lead times for the four types of MJO. First row: the observed composite anomalies of OLR (shading; W/m^2) and 850 hPa winds (m/s, not shown when wind speed is less than 0.5 m/s) averaged over days 1 to 5 for the four MJO clusters. The second to fifth rows are the composite results from model predictions with a lead time of 5 to 20 days, respectively. The black stippling denotes the regions with significant composite anomalies at the 10% significance level.

Accepted for publication in *Bulletin of the American Meteorological Society*. DOI 10.1175/BAMS-D-21-0124.1.

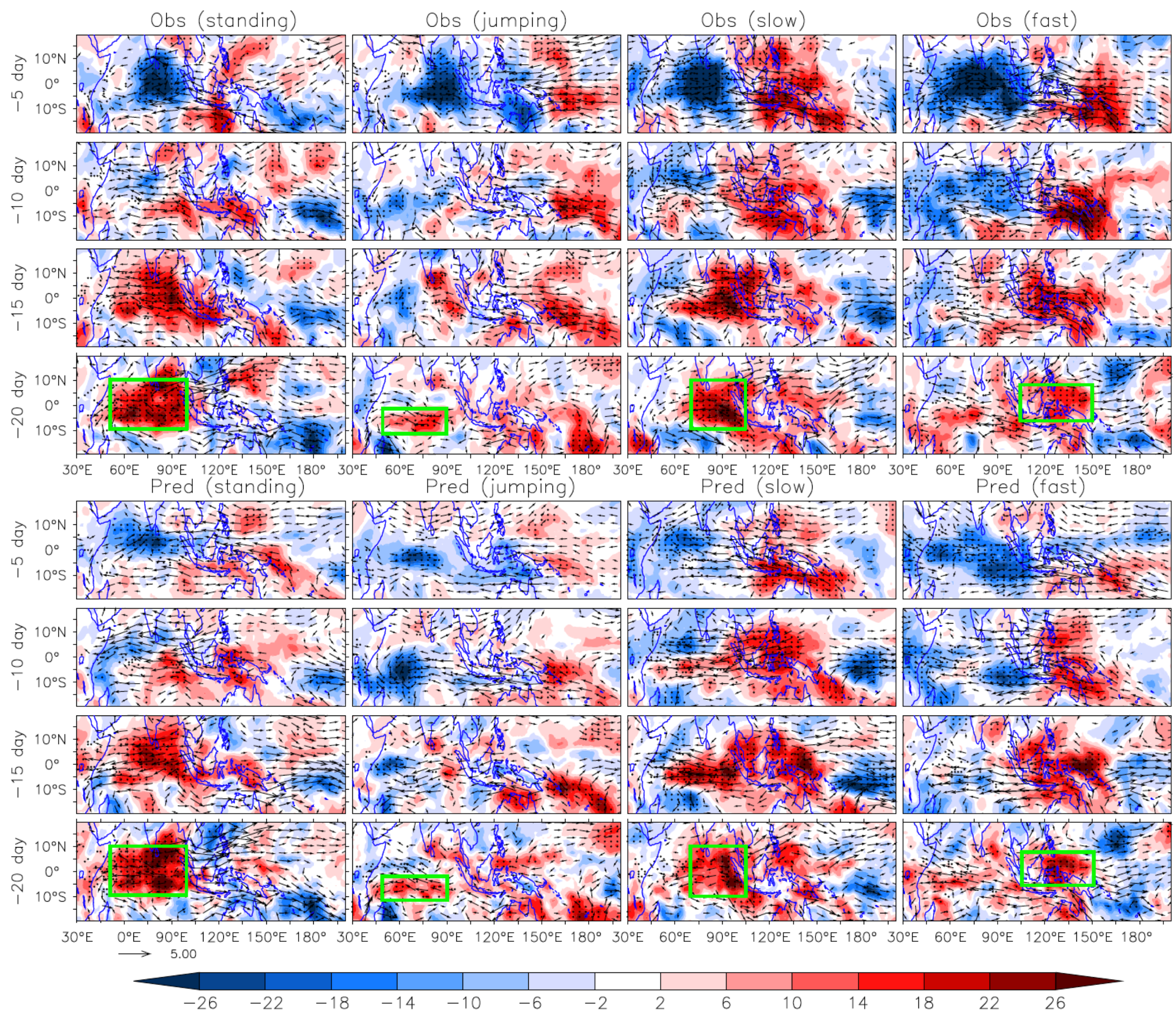

Figure 10 Observed precursors for the four types of MJO. First row: the observed composite anomalies of OLR (shading; W/m^2) and 850 hPa winds (m/s, not shown when wind speed is less than 0.5 m/s) averaged over the period between day -5 and day -1 for four MJO clusters. The second to fourth rows are similar but for 10, 15, and 20 days before the peak phase. The bottom four rows are similar but for the time evolutions of forecast initiated at day -20. The black stippling denotes the regions with significant OLR composite anomalies at the 10% significance level. Green boxes in the lowest panels for both observations and model forecast denote the key regions with precursory OLR signals.

Accepted for publication in *Bulletin of the American Meteorological Society*. DOI 10.1175/BAMS-D-21-0124.1.

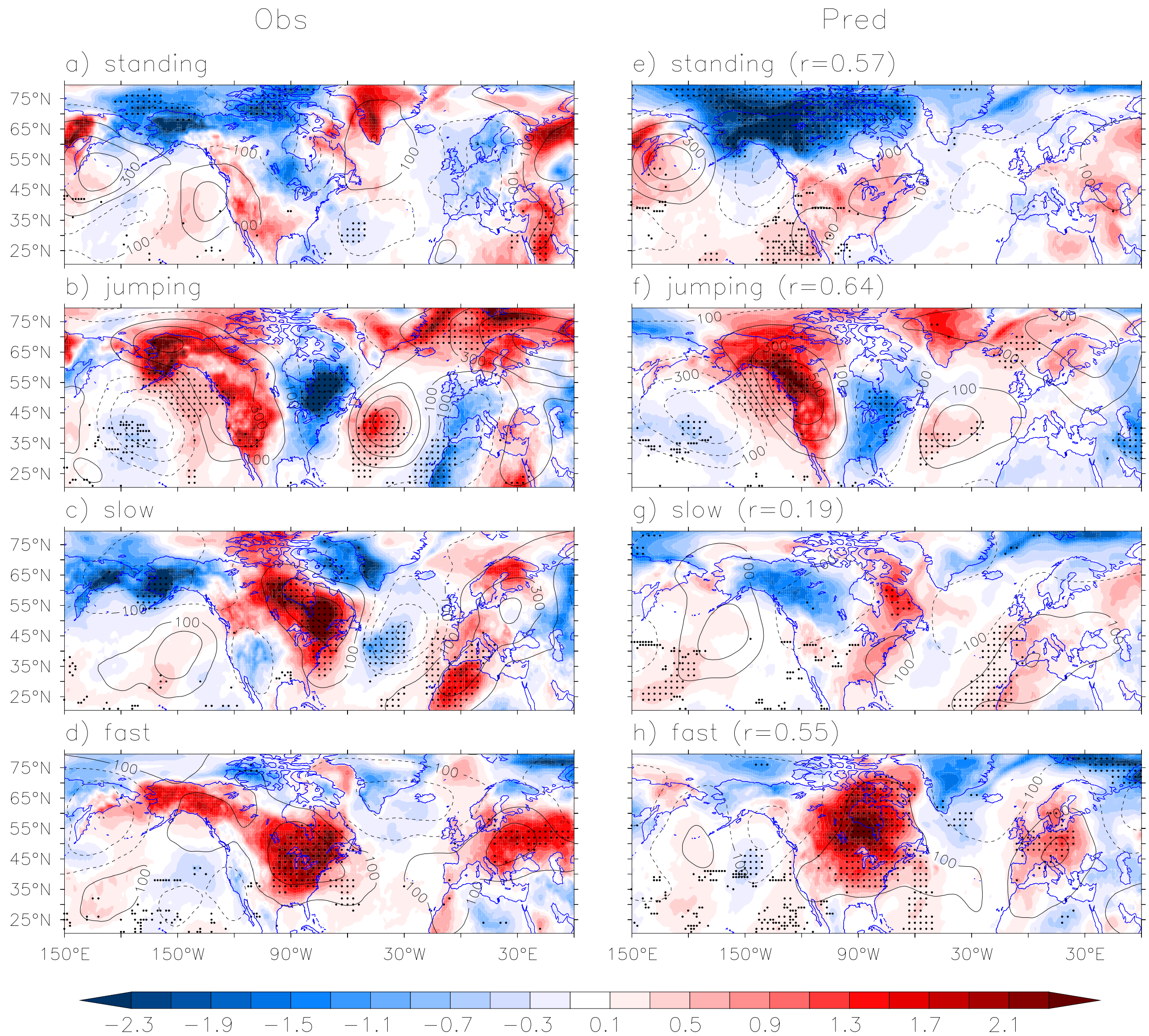

Figure 11 Observed and predicted teleconnection patterns associated with the four types of MJO. a-d) The composite observational anomalies of 2m temperature (shading; °C) and 500 hPa geopotential height (contours; m^2/s^2) averaged over 11 to 20 days after the peak phase (between day 11 and 20) for the four types of MJO, e-h) Similar to a-d) but for model predictions initiated at peak phase (around day 0). The correlation skills of 2m temperature anomalies are shown in parentheses.

Accepted for publication in *Bulletin of the American Meteorological Society*. DOI 10.1175/BAMS-D-21-0124.1.